Article

Skeletal muscle reprogramming enhances reinnervation after peripheral nerve injury

Pihu Mehrotra [1], James Jablonski[2], John Toftegaard[3], Yali Zhang[4], Shahryar Shahini[1], Jianmin Wang [4], Carey W. Hung[5], Reilly Ellis[5], Gabriella Kayal[5], Nika Rajabian [1], Song Liu[4], Kelly C. S. Roballo[5,6], Susan B. Udin [7], Stelios T. Andreadis [1,3,8,9] ✉ & Kirkwood E. Personius [2,9] ✉

Peripheral Nerve Injuries (PNI) affect more than 20 million Americans and severely impact quality of life by causing long-term disability. PNI is characterized by nerve degeneration distal to the site of nerve injury resulting in long periods of skeletal muscle denervation. During this period, muscle fibers atrophy and frequently become incapable of "accepting" innervation because of the slow speed of axon regeneration post injury. We hypothesize that reprogramming the skeletal muscle to an embryonic-like state may preserve its reinnervation capability following PNI. To this end, we generate a mouse model in which NANOG, a pluripotency-associated transcription factor is expressed locally upon delivery of doxycycline (Dox) in a polymeric vehicle. NANOG expression in the muscle upregulates the percentage of Pax7+ nuclei and expression of eMYHC along with other genes that are involved in muscle development. In a sciatic nerve transection model, NANOG expression leads to upregulation of key genes associated with myogenesis, neurogenesis and neuromuscular junction (NMJ) formation. Further, NANOG mice demonstrate extensive overlap between synaptic vesicles and NMJ acetylcholine receptors (AChRs) indicating restored innervation. Indeed, NANOG mice show greater improvement in motor function as compared to wild-type (WT) animals, as evidenced by improved toe-spread reflex, EMG responses and isometric force production. In conclusion, we demonstrate that reprogramming muscle can be an effective strategy to improve reinnervation and functional outcomes after PNI.

Peripheral Nerve Injuries (PNIs) refer to a range of sensorimotor impairments that occur when the peripheral nerves sustain damage or injury. These injuries are often the result of traumatic events like motor vehicle accidents, gunshot wounds, sports injuries, and combat wounds[1,2]. PNIs predominantly affect young, healthy males with an average age of 40 years, leading to significant morbidity and disability[1,3]. Surgical repair and reconstruction of damaged nerves pose significant clinical challenges, with less than half of the patients

[1]Department of Chemical and Biological Engineering, University at Buffalo, Buffalo, NY 14260, USA. [2]Department of Department of Rehabilitation Science, University at Buffalo, Buffalo, NY 14214, USA. [3]Department of Biomedical Engineering, University at Buffalo, NY, Buffalo, NY 14260, USA. [4]Department of Biostatistics and Bioinformatics, Roswell Park Comprehensive Cancer Center, Buffalo, NY 14203, USA. [5]Biomedical Affairs and Research, Edward Via College of Osteopathic Medicine, Blacksburg, VA 24060, USA. [6]Department of Biomedical Sciences and Pathobiology, Virginia Maryland College of Veterinary, Medicine, Virginia Tech, Blacksburg, VA 24060, USA. [7]Department of Physiology and Biophysics, Jacobs School of Medicine and Biomedical Sciences, University at Buffalo, Buffalo, NY 14203, USA. [8]Center of Excellence in Bioinformatics and Life Sciences, Buffalo, NY 14203, USA. [9]Center for Cell, Gene and Tissue Engineering (CGTE), University at Buffalo, Buffalo, NY 14260, USA. ✉e-mail: sandread@buffalo.edu; kep7@buffalo.edu

achieving normal sensory and motor function after nerve repair[4]. Patients with nerve injuries often experience chronic pain and persistent weakness, necessitating prolonged physical and occupational therapy for at least three months post-injury[5]. PNIs also impose a substantial economic burden on the US healthcare system, with an annual expenditure of approximately $150 billion, accounting for around 4.3% of total US health-related spending[1,6].

Over the past decades, the use of nerve grafts to repair nerve injuries has been the gold standard in the field. Autologous sensory or motor nerves can be harvested from a patient and sutured at the site of injury to bridge the defect. However, the supply of the autologous nerve is limited, and most often requires a secondary surgery increasing chances of donor site morbidity. Additional complications of nerve grafts include formation of painful neuromas, infection, and sensory loss[7,8]. Artificial nerve grafts or nerve conduits have been used as an alternative to autologous grafts and are commercially available and FDA approved[9]. The most commonly used materials include Type I Collagen[10], Chitosan[11,12], Polyglycolic acid (PGA)[13], Poly(dl-lactide-ε-caprolactone; PCL)[14] and Polyvinyl Alcohol (PVA)[9]. While nerve conduits show satisfactory recovery for nerve injuries, most FDA-approved grafts are only suitable for defects shorter than 3.0 cm in length and are not effective for critical long-gap nerve defects[15,16].

Nerve grafts can be decellularized to reduce immunogenicity while preserving the basement membrane and extracellular matrix (ECM) necessary for guiding axonal regeneration. However, acellular nerve grafts alone have not been as effective due to the absence of progenitor cells and Schwann cells that create a conducive microenvironment for regeneration[17]. Therefore, recent approaches focus on cellularizing grafts with specific cells that aid wound healing and nerve regeneration. Commonly used cell types for this purpose include Schwann cell presursors, Neural Stem cells, Bone Marrow-derived stem cells, Adipose-derived stem cells, and Skin-derived precursors. The use of these cells relies either on their ability to differentiate into functional Schwann cells at the injury site and/or secrete essential neurotrophic factors to facilitate axonal growth[18–20]. However, procuring these cells in a patient-specific manner to minimize immunogenic reactions has proven challenging[21].

As evident, most therapies to treat nerve injuries involve strategies to aid or accelerate nerve growth. The rate of human peripheral nerve regeneration is slow; approximately 1 inch per month[22]. As a result, skeletal muscle fibers remain denervated for long periods of time, leading to activation of atrophy related pathways, muscle wasting and ultimately loss of muscle function[23]. In fact, molecular changes in muscle function can be observed within a few hours of injury and denervation[24]. Consequently, by the time nerve endings reach the muscle for reinnervation, the muscle is severely atrophied and unable to 'accept' innervation[25]. Hence, finding ways to maintain the skeletal muscle in state that enables innervation might be crucial for better outcomes after PNIs.

Recent studies show that transient and partial reprogramming of cells or tissues using pluripotency factors can be an efficient way to enhance tissue regeneration while preventing teratomas[26]. In particular, Ocampo et al. showed that doxycycline (Dox)-inducible transient expression of four pluripotency genes- *Oct4*, *Sox2*, *Klf4* and *c-Myc* (OSKM) erased several signs of aging, prolonged lifespan and enhanced the regenerative capacity of aged tissues. Notably, they observed an increase in Pax7+ muscle cells and enhanced skeletal muscle regeneration after cardiotoxin (CTX) injury[27]. Virus-free expression of pluripotency factors using intramuscular delivery of plasmid encoding for OSKM also improved skeletal muscle regeneration[28]. In our lab, we have extensively studied the effect of pluripotency-associated transcription factor NANOG in enhancing regenerative capacity of tissues. NANOG expression in bone marrow-derived Mesenchymal Stem Cells (BM-MSC) from adult human donors could restore their myogenic differentiation potential and contractile properties that are otherwise impaired by senescence[29]. NANOG expression also restored synthesis of ECM, especially Collagen type III (Col3) in senescent human MSCs and progeric fibroblasts via the TGFβ pathway[30]. Subsequently, we found that transient expression of NANOG using a Dox-inducible system could restore the myogenic differentiation potential of skeletal myoblasts[31]. NANOG expression reversed the aged phenotype of senescent human myoblasts, as seen by enhanced cellular proliferation, heterochromatin modifications and decrease in DNA damage[32]. Further, NANOG expression restored skeletal muscle regeneration in-vivo in progeric mice. We observed an increase in Pax7+ satellite cells and embryonic myosin heavy chain positive (eMYHC+) myofibers after cardiotoxin injury in NANOG expressing progeric mice, along with an increase in skeletal muscle contraction force[33].

In all, we have established that transient NANOG expression enhances skeletal muscle regeneration capacity and confers a "young-like" state. Hence, we hypothesize that ectopic and transient NANOG expression may maintain the denervated skeletal muscle in a pro-regenerative state, and ultimately enable better reinnervation and enhanced functional outcomes post PNI.

Results

NANOG is expressed in skeletal muscle on Dox exposure through Elvax

To achieve skeletal muscle reprogramming using transient expression of NANOG, we used a transgenic mouse model, carrying the rtTA gene under the ROSA locus, and a cassette encoding for NANOG under the TetO promoter inserted in the Col1 locus. NANOG expression locally in the skeletal muscle was achieved using the slow-release polymer Elvax, impregnated with 25 mg Dox, that was implanted subcutaneously near the Tibialis Anterior (TA), Extensor Digitorum Longus (EDL), Soleus (Sol) and Gastrocnemius (GA) muscles (Fig. 1A, B; Supplementary Movie 1). EMG and strength assessments were performed in the TA muscle therefore, we limited our RNA and protein expression studies to the TA muscle. This focus allowed us to follow changes in RNA, protein, reinnervation and strength in a single muscle.

To assess the extent of NANOG expression in skeletal muscle following Elvax placement, we first implanted Elvax impregnated with Dox (Elvax-Dox) on the right leg of naïve non-injured WT and NANOG animals. The left leg of naïve NANOG animals underwent vehicle implantation (Elvax-DMSO), while the left leg of naïve WT animals did not (Supplementary Fig. 1A). To assess NANOG expression upon Dox administration, we performed RT-PCR with muscle tissues that were isolated after 4 days of Elvax placement. Indeed, the right TA muscle of NANOG mice showed ~800-fold increased mRNA levels of NANOG as compared to the left TA muscle, while NANOG expression remained unchanged in WT TA muscle on Dox administration (Fig. 1C). Immunohistochemistry for NANOG confirmed that NANOG was expressed in TA myofibers within 4 days of Dox-Elvax exposure, while no NANOG was expressed in the presence of DMSO-Elvax controls. Interestingly, we found that maximum NANOG expression was induced in nuclei of fibers on the surface of the muscle near where Elvax was placed. Some NANOG positive nuclei were also found within the center of the TA muscle (highlighted by white arrow, Fig. 1D). Elvax induced NANOG expression was not only limited to the TA muscle; Sol, GA and to a lesser extent, EDL also expressed NANOG. In fact, we found that NANOG expression was the greatest in the Sol muscle (124.18 ± 44.18-fold), followed by TA (15.81 ± 7.42-fold) and GA (14.22 ± 6.55-fold) muscles (Fig. 1E–I). The EDL muscle expressed very low levels of NANOG (8.20 ± 9.38-fold) that was not statistically significant.

NANOG expression reprograms skeletal muscle to a pro-regenerative state

To assess the ability of transient NANOG expression to induce skeletal muscle rejuvenation, the right leg of naïve ROSA-NANOG animals was

implanted with Dox-Elvax and the left leg with vehicle control DMSO-Elvax. After 2 weeks, the Elvax was removed and TA muscle was harvested 1 week later for evaluation of muscle structure, protein expression and markers of regeneration. We observed multiple small muscle fibers, especially close to the site of Dox-Elvax placement, suggesting skeletal muscle regeneration (Fig. 2A). These fibers were smaller than 500 μm² (Fig. 2B) and expressed eMYHC, an established marker of newly formed regenerative muscle fibers (Fig. 2A, C). Further, NANOG expression resulted in ~3-fold increase in centrally nucleated fibers throughout the muscle tissue (Fig. 2D). Immunostaining for the myogenic transcription factor Pax7 showed an increase in Pax7+ cells 1 week post Elvax removal. While the density of Pax7+ cells was higher at the edge of the muscle near the site of Elvax implantation, the percentage of Pax7+ cells was increased throughout

the NANOG expressing muscle (Fig. 2E, F). To verify that Elvax implantation did not cause any myofiber injury, and the small myofibers were indeed de-differentiated and not degenerated myofibers, we performed IgG uptake assay in these tissues. As a positive control, IgG staining was also performed after CTX injury (Supplementary Fig. 1B). IgG positive muscle fibers with central nuclei were evident following CTX injury. However, IgG positive muscle fibers were not seen after DMSO- or Dox-Elvax implantation. The small muscle fibers induced by transient NANOG expression following Dox-Elvax implantation did not show IgG staining indicating that these small fibers are not a result of myofiber injury (Supplementary Fig. 1B). Hence, transient NANOG expression induced fiber de-differentiation in an uninjured and non-denervated muscle, suggesting that it might reprogram the muscle to a state that enables re-innervation.
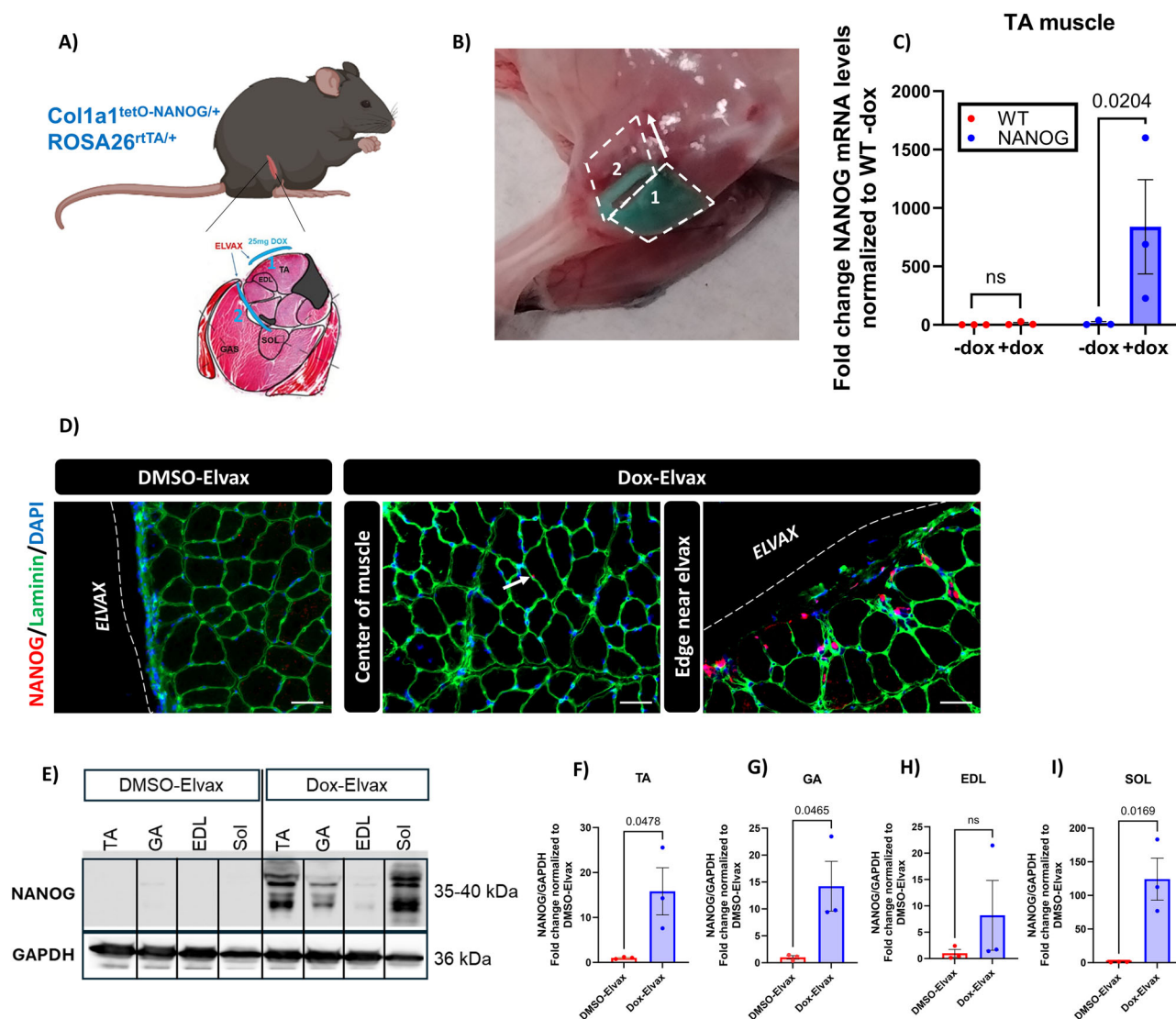

Fig. 1 | Mouse model for Dox-inducible NANOG expression in skeletal muscle.
A Localized NANOG expression in the muscle was achieved by subcutaneous implantation of the slow-release polymer Elvax (shown in blue) near the TA, EDL, Soleus and Gastrocnemius muscles. Schematic of muscle adapted from[123]. Figure created with BioRender.com. **B** Image showing two pieces of Elvax implanted in the mouse leg. Piece 1 induces Dox/DMSO delivery to the TA and EDL muscle. Piece 2 induces Dox/DMSO delivery to the GA and Sol muscles. **C** Fold change in relative mRNA levels of NANOG from isolated TA muscle 4 days after Elvax implantation in naïve uninjured WT and NANOG animals (n = 3 biological replicates, normalized to WT; no Elvax). Statistical test performed is two-way ANOVA with Uncorrected

Fisher's LSD test. **D** Immunostaining of TA muscle sections for NANOG (red), Laminin (green) and DAPI (Blue) 4 days after DMSO-Elvax or Dox-Elvax implantation. Scale bar = 50 μm. Fields of view depict representative images from the center of the muscle and section adjacent to Elvax placement. **E** Western blot for NANOG in TA, GA, EDL and Sol muscles 4 days after DMSO-Elvax and Dox-Elvax implantation. Fold change in NANOG expression in Dox-Elvax compared to DMSO-Elvax quantified after normalization to GAPDH in (**F**) TA (**G**) GA (**H**) EDL and (**I**) Sol muscles; n = 3 biological replicates for both DMSO-Elvax and Dox-Elvax. For G-I, unpaired t-test used for statistical analysis. All data are presented as Mean ± SEM. Source data are provided as a Source Data file.
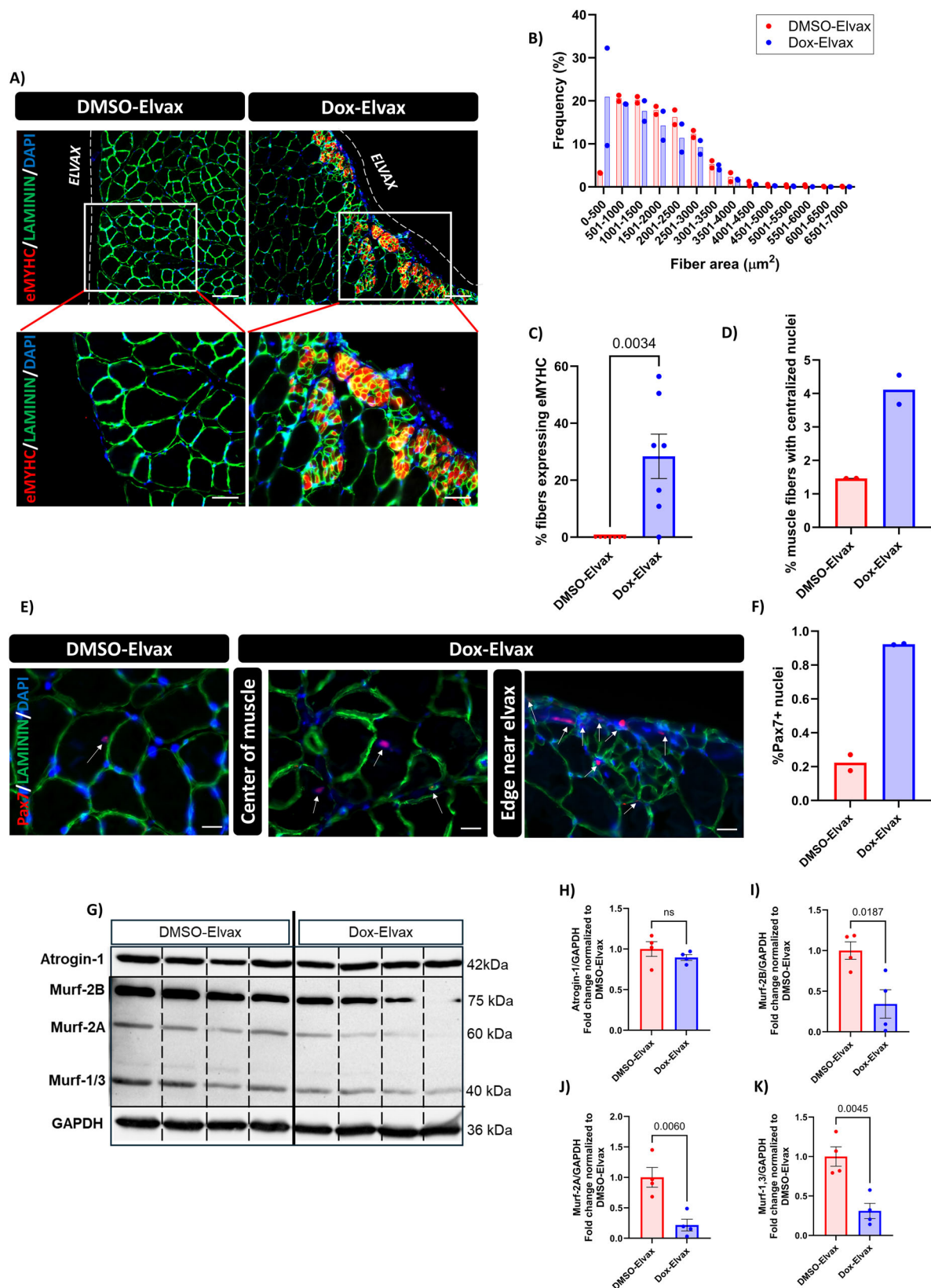
Previously, we have extensively studied the regenerative potential of the transcription factor NANOG in-vitro[32]. Human myoblasts were transduced with a lentiviral vector that encodes for NANOG under a tetracycline regulatable promoter (Supplementary Fig. 2A). NANOG was expressed for 5 days by treating cells with Dox, and RNA was isolated thereafter to assess changes in transcription. Interestingly, we found that transient NANOG expression in human myoblasts enriched key signaling pathways crucial for nerve development, regeneration, and synapse formation, such as NGF signaling pathway, NMDA receptor activation[34,35], neurotrophin signaling and neurotransmitter receptor binding (Supplementary Fig. 2B). Further, nerve associated genes such as NRG1, NRG2 and NGF were upregulated in human

Fig. 2 | NANOG expression de-differentiates skeletal muscle to a pro-regenerative state. The left leg of naïve uninjured mice was implanted with Dox-Elvax for two weeks; the right leg was implanted with DMSO-Elvax and served as control for the Elvax placement. One week after removal of Elvax, the TA muscle was harvested for evaluation. **A** Immunostaining of TA muscle sections for eMYHC (red), Laminin (green) and DAPI (Blue). Scale bar = 100 μm, insets are higher magnification images with scale bar = 50 μm. **B** Quantification of fiber area of TA muscle in mice with Elvax-DOX vs. Elvax-DMSO; $n = 2$ biological replicates for both DMSO-Elvax and Dox-Elvax, 200-250 muscle fibers from 3 muscle sections. **C** Quantification of small muscle fibers (less than 100 μm²) expressing eMYHC; $n = 7$ fields of view for 2 biological replicates for both DMSO-Elvax and Dox-Elvax. **D** Percentage of centrally nucleated regenerative muscle fibers throughout the TA muscle; $n = 2$ biological replicates for both DMSO-Elvax and Dox-Elvax, 200-250 muscle fibers per mouse. **E** Immunostaining for Pax7 (red), Laminin (green) and DAPI (blue). Fields of view depicted are representative images from the center of the muscle, and section adjacent to Elvax placement. Scale bar = 20 μm. **F** Quantification for percentage of Pax7 positive nuclei throughout the TA muscle; $n = 2$ biological replicates for both DMSO-Elvax and Dox-Elvax. **G** Western blot for atrogenes Atrogin-1 and Murf-2B, Murf-2A and Murf-1/3 in the TA muscle. Fold change in (**H**) Atrogin-1 (**I**) Murf-2B (**J**) Murf-2A and (**K**) Murf-1/3 expression in Dox-Elvax compared to DMSO-Elvax quantified after normalization to GAPDH; $n = 4$ biological replicates for both DMSO-Elvax and Dox-Elvax. Unpaired t-test used for statistical analysis in all graphs. All data are presented as Mean ± SEM. Source data are provided as a Source Data file.

skeletal muscle cells that expressed NANOG. Additionally, NANOG significantly downregulated Atrogin-1 and Murf-1, key genes associated with skeletal muscle atrophy in human myoblasts in-vitro (Supplementary Fig. 2C). Interestingly, we found that Elvax-Dox implantation also decreased some markers of atrophy 1 week after Elvax removal. Specifically, NANOG expression significantly decreased protein levels of Murf-2B, Murf-1/3 and Murf-2A, though we did not see any change in Atrogin-1 expression (Fig. 2G–K). These findings prompted us to examine whether NANOG expression in skeletal muscle promoted innervation, neuromuscular junction formation, and functional recovery after nerve injury.

NANOG expression in denervated muscle upregulates key genes associated with skeletal muscle development and nerve growth

To understand the effect of skeletal muscle NANOG expression on peripheral nerve regeneration and synapse formation after nerve injury, we performed complete nerve transection of the right sciatic nerve followed by an end-to-end suture. At the same time, Elvax-Dox was implanted subcutaneously at the right skeletal muscle of NANOG and WT animals. The left sciatic nerve was left non-transected and served as an internal control for each animal. Elvax was removed after 2 weeks of nerve transection, and recovery was monitored over 16 weeks. Nerve and muscle tissues were isolated after 5 weeks and 16 weeks for RNA and protein isolation and immunocytochemistry analysis (Fig. 3A).

Interestingly, RNA sequencing analysis on the TA muscle tissue 5 weeks post PNI revealed that the top 42 upregulated genes were common in both WT and NANOG animals. However, the extent of upregulation of these genes was higher in NANOG animals (Fig. 3B). Specifically, we noticed that key genes related to embryonic muscle development and nerve regeneration were upregulated to a significantly greater extent upon NANOG expression. Myomarker (MYMK) and Myomixer (MYMX) govern muscle fusion and are essential genes involved in skeletal muscle regeneration during embryo development and in response to injury[36,37]. Neuregulin-2 (NRG2) is a nerve growth factor widely implicated in neuromuscular synapse formation[38,39]. CHRNG encodes for an acetylcholine receptor isoform that is expressed in fetal and denervated but not in adult muscle and plays a key role in formation of the motor endplate[40]. GDF15, NRCAM and SOX11 are involved in nerve development and subsequent synaptogenesis[41–44]. Lastly, GDF5 has been shown to suppress denervation related muscle atrophy[45]. While all these genes were upregulated after transection in both WT and NANOG mice, the extent of upregulation was significantly higher after NANOG expression (Fig. 3C). We further confirmed this by RT-PCR analysis on TA muscle isolated from NANOG and WT animals at 5 weeks post transection. Indeed, expression of MYMK, NRG2, CHRNG, NRCAM, SOX11 and GDF5 was significantly upregulated in NANOG mice, while MYMX and GDF15 also increased although not significantly (Fig. 3D).

Upregulated genes in the transected leg of NANOG animals were then annotated based on their function using Gene ontology (GO) enrichment analysis. Key genes associated with Axon guidance such as

NGFR, Plxnb1, Plxnb2, Bmp7 and Erbb2[46–49], as well as those implicated in skeletal system morphogenesis such as Bmp7, Bmp4, Pdgfrb, Wnt10b and Myf5[50–53] were upregulated in NANOG compared to WT animals at 5 weeks after transection (Fig. 3E, F; green boxes denote key genes).

In all, NANOG expression in the skeletal muscle upregulates genes that are implicated in three aspects of muscle function: (i) muscle development often during embryogenesis; (ii) nerve and synapse development; and (iii) skeletal muscle hypertrophy.

NANOG expression enhanced gene pathways involved in ECM remodeling and nerve regeneration and increases myofiber cross section area 5 weeks after nerve injury

To further evaluate the transcriptional effects of NANOG expression on the skeletal muscle, we performed Gene Set Enrichment Analysis (GSEA) and GO analysis using RNA isolated from the TA muscle at 5 weeks post transection. GO analysis revealed that pathways (cellular components, molecular functions, and biological processes) related to ECM synthesis and signaling, such as collagen formation and binding, and elastin assembly were among the top 10 most highly upregulated pathways in NANOG compared to WT mice at 5 weeks after nerve transection (Fig. 4A; red bars). Further, multiple pathways related to nerve regeneration, such as Tyrosine Kinase Receptor activity, and platelet-derived growth factor (PDGF) signaling were also upregulated by NANOG (Fig. 4A; green bars).

Interestingly the GO pathway "Synapse" was significantly enriched (Fold enrichment: 1.53, FDR: <0.0001) with NANOG (Supplementary Fig. 3A). The key gene AGRN that has been extensively shown to be critical for formation of neuromuscular synapses[54–56] was upregulated by NANOG. Other genes critical for synapse formation and function such as Nlgn2[57], Clcn5[58], Sv2c[59], and Th[60] were also upregulated by NANOG (Supplementary Fig. 3A; green arrows). Other significantly enriched GO terms included "Innervation"; (Fold enrichment: 5.19, FDR: 0.0047) (Supplementary Fig. 3B), "Distal Axon"; (Fold enrichment: 2.20, FDR: 0.0004) (Supplementary Fig. 3C), "Cellular Response to PDGF Stimulus"; (Fold enrichment: 6.70, FDR: 0.0043) (Supplementary Fig. 3D), "Semaphorin-Plexin signaling pathway involved in Axon Guidance"; (Fold enrichment: 8.37, FDR: 0.0024) (Supplementary Fig. 3E), "Nerve Development"; (Fold enrichment: 3.65, FDR: 0.0009) (Supplementary Fig. 3F), "Skeletal System Development"; (Fold enrichment: 2.84, FDR: <0.0001) (Supplementary Fig. 3G) and "Collagen Fibril Organization"; (Fold enrichment: 11.63, FDR: <0.0001) (Supplementary Fig. 3H). Most of these pathways have been previously implicated in aiding nerve regeneration and repair after PNI[61–63].

Gene Set Enrichment Analysis further confirmed this result; 80% of the top 20 most highly upregulated pathways by NANOG were associated with ECM organization and signaling upon nerve transection, while these pathways comprised only 10% of all the pathways upregulated in WT transected muscle (Supplementary Fig. 4A–C). Specifically, Reactome database pathways correlated with ECM organization; Extracellular Matrix Organization, Collagen Formation,
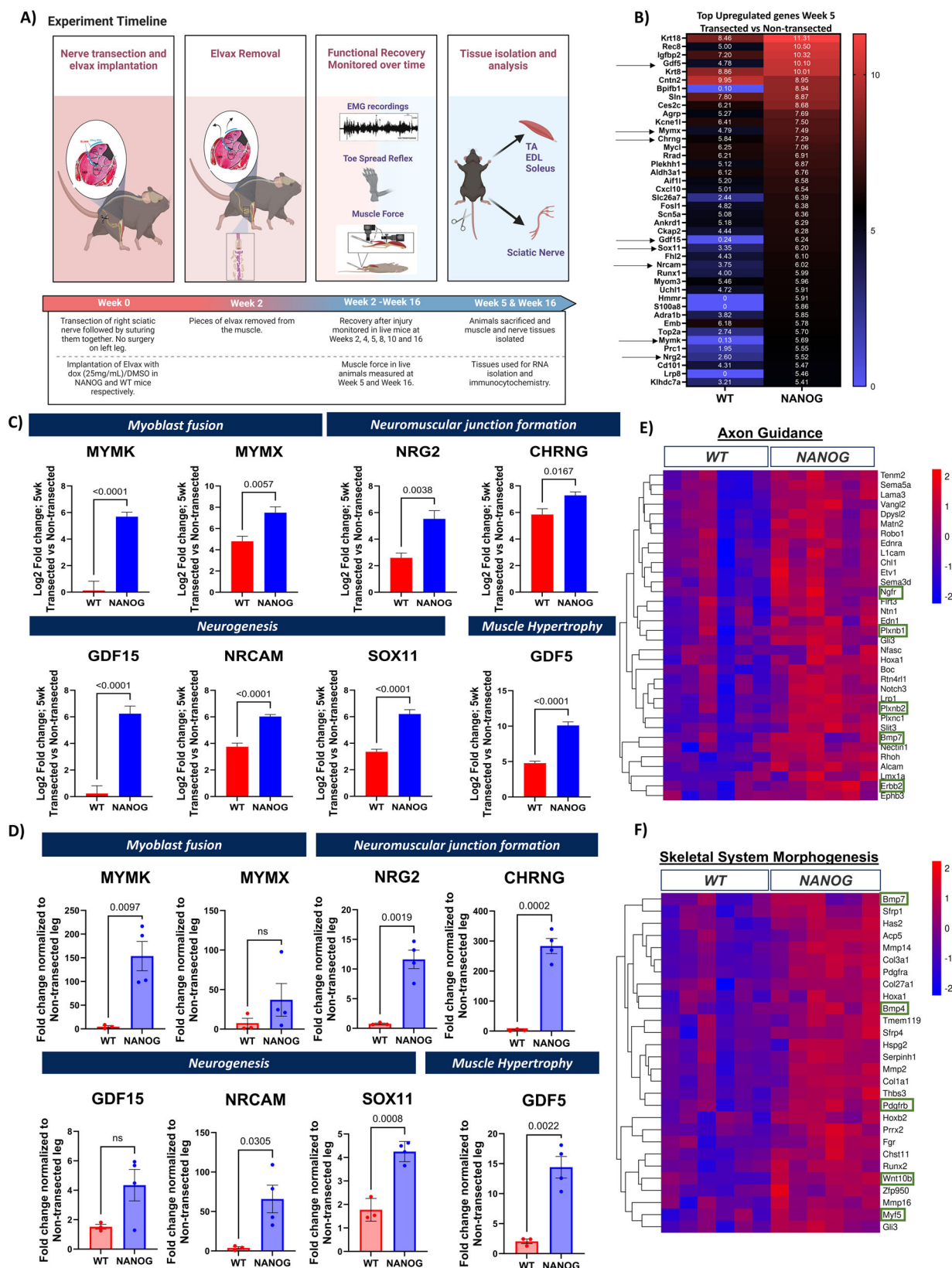
Integrin Cell Surface Interactions, and ECM Proteoglycans were significantly enriched by NANOG (Fig. 4B). Additionally, KEGG database pathways pertaining to Axon Guidance, Gap junction and Neuroactive Ligand receptor Interaction, and the Reactome pathway NCAM Signaling for Neurite Outgrowth was upregulated in the muscle of NANOG animals at 5 weeks after injury (Fig. 4C). While we did observe

upregulation of some ECM and nerve related pathways at 16 weeks after transection (Supplementary Fig. 4D), the transcriptional changes were not as pronounced as on week 5. We did not observe any upregulation of embryonically relevant genes such as MYMK, MYMX and CHRNG at 16 weeks after transection, indicating that the muscle had approached its homeostatic state.

Fig. 3 | NANOG expression in skeletal muscle in a sciatic nerve injury model upregulates genes associated with skeletal muscle dedifferentiation, neurogenesis and nerve development 5 weeks post injury. A Schematic depicting experimental procedure, timeline and experiments performed. Figure created with BioRender.com. **B** Top 42 upregulated genes in TA muscle on side of transection normalized to non-transected limb in WT and NANOG animals. Log2 fold change values are depicted within each cell. Genes of interest with respect to muscle or nerve development are highlighted by arrows. **C** Plot depicting mean log 2-fold change in selected genes from **B** associated with myoblast fusion (MYMK and MYMX), NMJ formation (NRG2 and CHRNG), neurogenesis (GDF15, NRCAM and Sox11) and muscle hypertrophy (GDF5) after transection, normalized to expression in non-transected limb of the same animal in WT and NANOG mice. $n = 5$ biological replicates for WT, $n = 6$ biological replicates for NANOG. **D** RT-PCR expression data from TA muscle for genes in **C** on side of transection normalized to non-transected limb in WT and NANOG animals; $n = 3$ biological replicates for WT, $n = 4$ biological replicates for NANOG. **E** Heatmaps showing differentially expressed genes associated with gene ontology term Axon Guidance and **F** Skeletal System Morphogenesis. Only genes with statistically significant differences (padj<0.05) between WT and NANOG samples have been depicted. Genes of particular interest are highlighted within green boxes; $n = 6$ biological replicates for both WT and NANOG mice. Unpaired t-test used for statistical analysis in all graphs. All data are presented as Mean ± SEM. Source data are provided as a Source Data file.

Further, we observed that NANOG expression downregulated key pathways and proteins associated with skeletal muscle atrophy. GO analysis revealed that the top 10 downregulated cellular components, molecular functions, and biological processes upon NANOG expression comprised of pathways associated with the Ubiquitin Proteosome System and Autophagy-related pathways (Supplementary Fig. 5A, Supplementary Fig. 3I, J). GSEA enrichment analysis also revealed that the KEGG pathway correlated with Ubiquitin Mediated Proteolysis and Reactome database pathway correlated with Autophagy were significantly downregulated after 5 weeks of transection in NANOG mice (Supplementary Fig. 5B). Both pathways have been shown to play important roles in mediating muscle wasting[64–67]. However, we did not see any differences in protein levels of key genes associated with these pathways at the 5-week time point. Specifically, expression of atrophy genes associated with the Ubiquitin Proteosome Pathway such as MSTN, Murf-2 (Supplementary Fig. 5C–E), Atrogin-1 (Supplementary Fig. 5F, G) and total and p-FOXO1 (Supplementary Fig. 5H–J) remained unchanged in WT and NANOG transected ends in the TA muscle. Further, we also did not find any difference in expression of autophagy related genes such as LC3A/B and P62 (Supplementary Fig. 5K–M) and MYH (Supplementary Fig. 5N, O) in WT and NANOG transected muscle.

RNA sequencing data also revealed that NANOG expression suppressed mitochondrial pathways 5 weeks after nerve injury (Supplementary Fig. 5A). Several studies in literature suggest that denervation-induced muscle atrophy leads to an increase in mitochondrial reactive oxygen species (ROS) production leading to mitochondrial damage[68–70]. To assess if NANOG expression leads to changes in ROS levels, we analyzed total ROS in WT Transected, NANOG Transected and Control Non-Transected GA muscle 5 weeks post nerve transection. Interestingly, we found that nerve transection in WT animals led to a significant increase in ROS levels. However, NANOG animals showed decreased ROS accumulation 5 weeks after denervation, to similar levels as non-transected controls (Supplementary Fig. 5P).
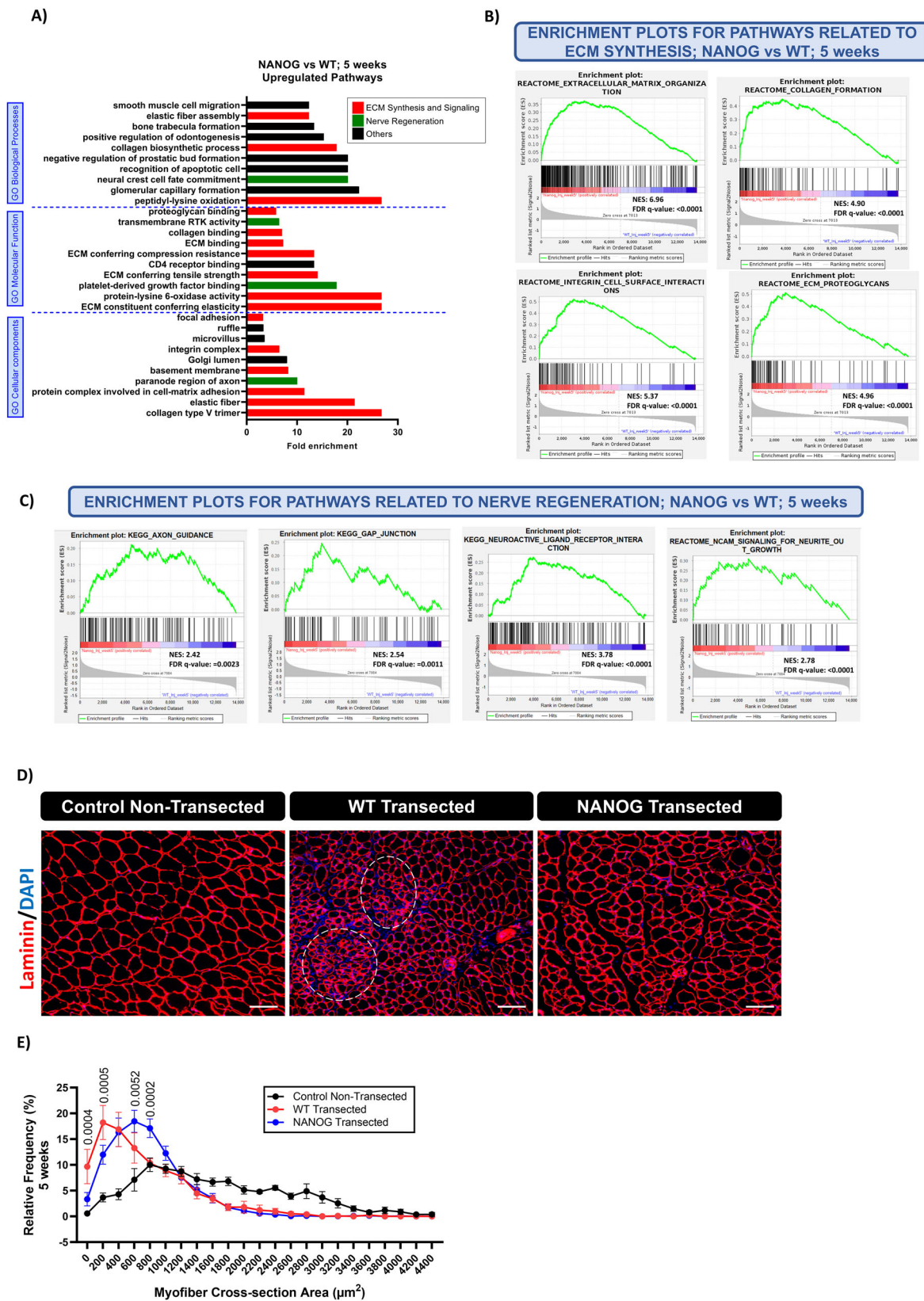
Interestingly, while we did not observe any change in expression of atrogenes at 5 weeks after injury, functional marker of muscle atrophy such as muscle cross-sectional area was significantly different in WT and NANOG mice. Specifically, we found that NANOG expression in the skeletal muscle led to recovery of myofiber area 5 weeks post nerve transection, as seen by a decrease in number of small, degenerated fibers (<400 μm²; highlighted in areas within white circle), and an increase in the number of larger fibers (400–1000 μm²; Fig. 4D, E). However, by 16 weeks, the muscle cross section area was recovered in WT mice, and we did not find any difference in myofiber area among WT Transected, NANOG Transected and Control Non-Transected TA muscle (Supplementary Fig. 6A, B).

These data suggest that NANOG expression alters the ECM landscape of the muscle, potentially aiding synaptogenesis and effective development and maturation of NMJs[71]. Further, essential neuronal signaling events that are important to establish synapses and aid nerve regeneration such as neuronal cell-adhesion molecules (NCAMs)[72] are enhanced by NANOG, ultimately resulting in enhanced myofiber cross sectional area. Collectively, these data suggest that NANOG expression might prime the skeletal muscle for enhanced re-innervation.

NANOG expression enhanced neuromuscular junction formation

To assess the effect of NANOG expression on structural changes in the reinnervated neuromuscular junction, we performed whole muscle immunohistochemistry in EDL and soleus muscles at 5 and 16 after sciatic nerve transection. The presynaptic axons (nerve filaments) and synaptic vesicles (SVs) were co-labelled, and their co-localization to postsynaptic AChRs was evaluated. In the muscles of control non-transected limb, the SVs were nearly completely colocalized with AChRs, and innervation of each NMJ was achieved by a single motor neuron (Fig. 5A). Overlap between AChRs and SV2 was significantly decreased in WT animals as compared to non-transected controls at 5 weeks after nerve transection. Notably, we did not find any significant differences in overlap between non-transected controls and NANOG animals 5 weeks after transection. Overlap was significantly decreased between non-transected controls and WT mice at 5-weeks (Control Non-transected: 71.8 ± 6.18%; NANOG: 57.2 ± 18.24%, WT: 42.28 ± 22.7%, One-way ANOVA and Tukey's post-hoc test; $p = 0.002$; Fig. 5A, B). This trend continued at 16 weeks post injury, with significantly decreased overlap in WT mice (53.6 ± 20.83%) as compared to NANOG mice (66.12 ± 17.44 %, $p = 0.02$) (Fig. 5A, C). Interestingly, neuromuscular junctions of WT mice were frequently innervated by multiple axons at 5- and 16-weeks post injury (asterisk), indicating an immature state of innervation[73] (Fig. 5A). To further investigate NMJ morphology, we used the publicly available NMJ-morph tool[74] to calculate AChR area, AChR perimeter, Endplate area, Fragmentation, Average area of AChR clusters, Compactness, Nerve terminal area, Axon Diameter, Number of terminal branches, and Number of branch points at 5 weeks (Supplementary Fig. 7A) and 16 weeks (Supplementary Fig. 7B) post nerve injury. Many morphologic parameters were unaffected by NANOG, but the endplate region was more fragmented in NANOG mice at 5 weeks (Supplementary Fig. 7A). Interestingly, dystrophic muscle, which is in a constant state of de-differentiation and regeneration also has increased AChR fragmentation[75]. By 16 week, Nerve terminal area, Number of terminal branches, and Number of branch points were increased in NANOG mice, indicating improved pre-synaptic reinnervation (Supplementary Fig. 7B)[76].

Whole mount immunohistochemistry only allows assessment of NMJs on the surface of the muscle fibers. To assess innervation throughout the entire muscle, we quantified colocalization between AChRs and SV2 in TA muscle cross-sections (Fig. 5D). While there was no significant difference in overlap between WT and NANOG animals at 5 weeks post transection (Fig. 5D, E), NANOG mice showed significantly improved overlap as compared to WT mice by 16 weeks (Control Non-transected: 78.47 ± 22.02% NANOG: 72.91 ± 26.43%; WT: 59.32 ± 30.81%; One-way ANOVA and Tukey's post-hoc test; $p < 0.0001$; Fig. 5D, F). Interestingly the extent of overlap was similar at 5 weeks and 16 weeks in WT mice, suggesting that structural reinnervation showed limited improvement after 5 weeks. Taken together, these findings demonstrate that NANOG expression in the muscle enhanced NMJ formation and restored innervation, indicating efficient reinnervation after PNI.

A) NANOG vs WT; 5 weeks Upregulated Pathways

B) ENRICHMENT PLOTS FOR PATHWAYS RELATED TO ECM SYNTHESIS; NANOG vs WT; 5 weeks

C) ENRICHMENT PLOTS FOR PATHWAYS RELATED TO NERVE REGENERATION; NANOG vs WT; 5 weeks

D) Control Non-Transected / WT Transected / NANOG Transected — Laminin/DAPI

E)

NANOG upregulated myelination related pathways within the muscle but not fluoromyelin content of the sciatic nerve axon

Given the enhanced NMJ formation in NANOG animals post nerve transection, we were curious about the structural integrity and myelination levels of the sciatic nerve. GO pathway analysis revealed that key genes associated with gliogenesis (Fold enrichment: 2.68, FDR: <0.0001), glial cell migration (Fold enrichment: 4.66, FDR: 0.0020) and myelin assembly (Fold enrichment: 6.43, FDR: 0.0022) were upregulated by NANOG (Supplementary Fig. 8A–C). Further, GSEA analysis revealed that the Reactome pathway "EGR2 and Sox10 mediated initiation of Schwann Cell Myelination" was also significantly enriched in NANOG animals 5 weeks post injury (Supplementary

Fig. 4 | NANOG upregulates ECM organization and Nerve Regeneration pathways and increases myofiber cross section area 5 weeks after nerve injury.
A Top 10 most highly enriched GO cellular components, molecular functions and biological processes 5 weeks after PNI. ECM: Extracellular Matrix, RTK: Receptor Tyrosine Kinase. **B** Enrichment plots from Reactome database depicting ECM synthesis and signaling associated pathways; ECM organization, Collagen formation, Integrin cell surface interactions and ECM proteoglycans. **C** Enrichment plots from KEGG and Reactome databases depicting nerve development pathways; Axon guidance, Gap junction, Neuroactive ligand receptor interaction and NCAM signaling for neurite outgrowth; $n = 6$ biological replicates for both WT and NANOG.

D Immunostaining of TA muscle sections for Laminin (red) and DAPI (Blue) 5 weeks after nerve injury. Scale bar = 100 μm. Areas within white circles depict atrophied muscle fibers. **E** Quantification for myofiber cross sectional area in WT transected, NANOG Transected and Control Non-Transected muscle; $n = 6$ biological replicates for all groups- Control non-transected, WT transected and NANOG transected, 200-250 muscle fibers per mouse. Data is presented as Mean ± SEM. Statistical analysis performed using two-way ANOVA with Tukey's multiple comparison test. *P*-values depicted in the plot represent statistically significant differences in WT transected and NANOG transected groups. Source data are provided as a Source Data file.

Fig. 8D). To assess changes in myelination, we isolated the sciatic nerve at the site of transection from both non-transected and transected legs of WT and NANOG animals 5 weeks post injury and stained for myelin using fluoromyelin red (Supplementary Fig. 8E, F). We did not observe any change in fluoromyelin red stain intensity within axon of the transected NANOG nerve (31.93 ± 10.29) compared to the transected WT nerve (21.50 ± 3.58) and control non-transected nerve (29.12 ± 11.65; Supplementary Fig. 8G). In all, this suggests that effects of Elvax-induced NANOG expression are restricted to the skeletal muscle. While NANOG increases transcription of some myelination-associated pathways within denervated muscle, it does not induce gross increases in remyelination of axons at the site of nerve transection 5 weeks post injury.

NANOG expression improved toe spread reflex, electromyographic (EMG) compound muscle action potential (CMAP) and muscle isometric force production

Functional recovery after nerve transection was investigated throughout 16 weeks of recovery. First, we ranked the toe-spread reflex in WT and NANOG animals after nerve transection. The return of toe spread reflex is a more sensitive measure of restored function than analysis of gait following sciatic nerve injury[77,78]. The reflex was scored between 0-2; 0 indicating no spreading, 1 indicating intermediate spreading, and 2 indicating complete spreading of the toes (Fig. 6A). The toe-spread score in WT mice improved up to Week 4 and plateaued thereafter. However, the toe-spread score in NANOG mice increased continually over 16 weeks and was significantly higher compared to WT mice from 8–16 weeks (Two-way ANOVA and Tukey's post-hoc test; $p = 0.0004$; Fig. 6B).

Next, we performed needle EMG recordings to measure the summated action potentials of all stimulated motor endplates within the TA muscle. Stimulating electrodes were placed on either side of the sciatic nerve proximal to the site of transection and the CMAP M-wave was recorded via an electrode placed at the mid-belly of the TA muscle (Fig. 6C, D). As seen in the representative EMG CMAP, the transected leg of the NANOG mice produced a stronger and well-developed M-wave (arrows) resembling the recording in non-transected control. The EMG CMAP captured in WT mice showed weak muscle activation upon stimulation at both 5- and 16-weeks post nerve transection (Fig. 6E). The CMAP waveforms were quantified based on amplitude (peak to peak) and area (under the waveform), both of which are indicators of synaptic strength[79] (Fig. 6 F, J). EMG recordings were performed on transected and non-transected limbs for every animal at each time-point. Thus, all data was plotted as the ratio of transected to non-transected limb. By 5 weeks, WT mice showed limited reinnervation (2.3 ± 0.7% of non-transected control limb), while EMG CMAP amplitude significantly recovered to 14.2 ± 4.0% of the non-transected limb in NANOG mice. EMG amplitude continued to improve to 64.3 ± 9.2% of the non-transected limb by 16 weeks in NANOG mice, while recovery stalled at 21.7 ± 9.9% of the non-transected limb in WT mice (Two-way ANOVA and Tukey's post-hoc test; $p = 0.0022$; Fig. 6G). In fact, the amplitude of M-wave in NANOG mice was improved by almost 7-fold as early as 5-weeks (Fig. 6H), and the difference remained statistically

significant at 16 weeks (Fig. 6I). The CMAP area followed a similar trend (Fig. 6J), reaching greater area in NANOG mice, but stagnating after 8 weeks in WT mice (Two-way ANOVA and Tukey's post-hoc test; $p = 0.0105$; Fig. 6K). We found a 7-fold increase in area at 5 weeks (Fig. 6L) and 2-fold increase at 16 weeks (Fig. 6M) in NANOG animals.

We also quantified the onset latency time, which is determined by the time taken from the stimulus artifact to the onset of CMAP depolarization response[80] (Fig. 6N). Increased latency time indicates a slower axon conduction speed of the fastest axons. Interestingly, NANOG mice had significantly lower latency time as early as 2 weeks after transection. The latency time in WT mice improved between 5 to 8 weeks post transection but did not improve further (Two-way ANOVA and Tukey's post-hoc test; $p > 0.05$; Fig. 6O). While we did not find significant differences in latency time of WT and NANOG animals 5 weeks after transection (Fig. 6P), the latency time of NANOG animals after 16 weeks was significantly lower (Fig. 6Q). Taken together, these data suggest that NANOG animals exhibited improved reinnervation and formed functional synapses after sciatic nerve transection / repair. While WT animals were capable of reinnervation, but the recovery of EMG CMAP stagnated after 5-8 weeks.

Next, we measured isometric muscle force in transected and non-transected legs of live animals at 5 and 16 weeks after transection. Each animal was anesthetized while its foot was attached to a footplate fastened to a dual-mode lever. The TA muscle was stimulated by using subcutaneous EMG electrodes, and the aggregate torque produced was quantified as force generated by the muscle (Fig. 6R). We found that the ratio of the force exerted by the transected over the non-transected limb was significantly higher in NANOG as compared to WT mice at both 5 weeks (NANOG: 39.8 ± 5.1%; WT: 29.1 ± 5.6%; Fig. 6S) and 16 weeks (NANOG: 98.8 ± 10.4%; WT: 73.2 ± 13.1%; Fig. 6T). In all, we demonstrate that enhanced innervation is accompanied by enhanced muscle function, evidenced by complete recovery in isometric force production in NANOG mice.

Discussion

Nerve injuries affect primarily young individuals, who potentially suffer for multiple decades after the injury[81]. For humans, 12 to 18 months is the accepted window within which reinnervation must occur to achieve partial functional recovery before degeneration of the motor end plate is irreversible[82]. However, nerve lesions are often diagnosed after significant delay, leaving a short time for adequate treatment[83]. As a result, only partial recovery is achieved post PNI, and many patients experience limited mobility and chronic debilitating pain[84]. Most current approaches to treat nerve injuries rely on developing biomaterial scaffolds to bridge the nerve gap[85] or using Schwann cells to aid nerve regeneration[86]. However, none of these current approaches address the worsening stromal environment of the muscle, often caused by slow rate of nerve growth and delayed medical intervention. Long-term muscle denervation induces motor endplates to be non-permissive to axonal innervation resulting in a non-functional synapse[25].

In this study, we demonstrate a novel approach to improve functional outcomes after PNI. We use a transgenic mouse model to
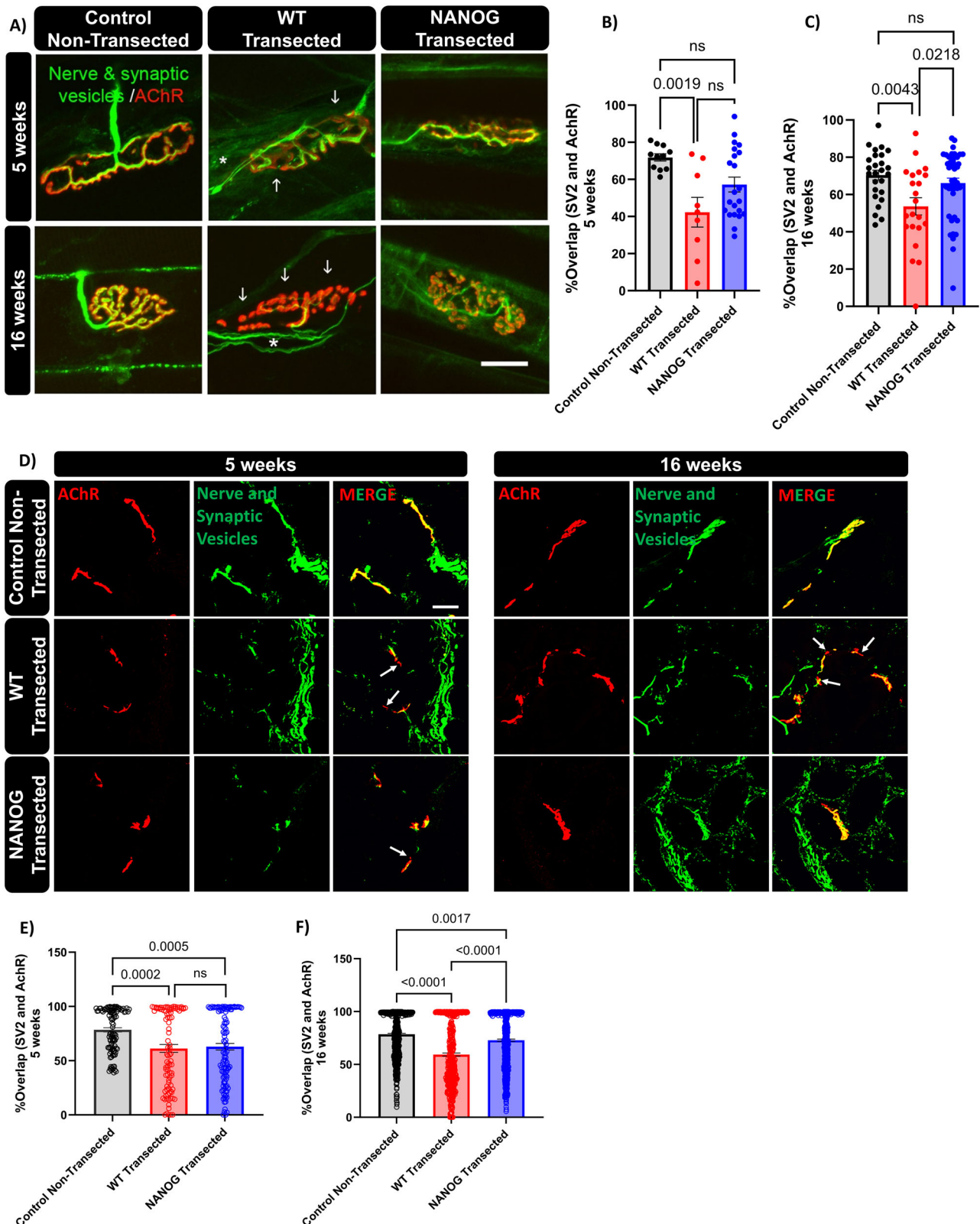
partially reprogram the skeletal muscle by expressing the embryonic transcription factor NANOG. Muscle specific NANOG expression was achieved using the slow-release polymer Elvax (ethylene-vinyl acetate copolymer), that has been extensively used as an implantable slow-release drug delivery agent[87,88]. In the past, Elvax has been used for the delivery of low molecular weight compounds such as glutamate receptor antagonists[89-91], and the release profile of these drugs from

Elvax has been characterized as an initial burst of release for 2 weeks, followed by slow decline in release rate over the next six weeks[92].

Partial reprogramming has been used to reverse the hallmarks of aging while avoiding the risk of teratoma formation and preventing loss of tissue identity and function[93]. We have previously shown that transient NANOG expression could rejuvenate aged skeletal muscle and enhance muscle force[33]. In this study, we show that partial

Fig. 5 | NANOG improves overlap between neuronal synaptic vesicles and muscle AChRs following transection. A Confocal images of NMJs 5 and 16 weeks after transection using whole mount immunocytochemistry labeled for presynaptic axons and synaptic vesicles (green) and postsynaptic AChRs (Red). Regions of overlap between pre- and post-synaptic regions are yellow. WT mice frequently demonstrate poor overlap between synaptic vesicles and AChRs (arrows). Multiple innervations were also seen in WT mice (asterisks). NANOG mice showed pre- vs. post-synaptic overlap similar to NMJs from control non-transected limbs. Scale bar = 20 μm. Quantification for percentage of colocalization between synaptic vesicles and AChRs at (**B**) 5 weeks and (**C**) at 16 weeks; each point in the dispersion plot represents a single NMJ from n = 6 biological replicates per condition. For 5 weeks dataset: n = 11 for Control Non-Transected, n = 9 for WT Transected, n = 22 for NANOG Transected. For 16 weeks dataset: n = 26 for Control non-transected, n = 22 for WT transected, n = 45 for NANOG transected. **D** Confocal images of NMJs 5 and 16 weeks after transection in muscle cross-sections labeled for presynaptic axons and synaptic vesicles (green) and postsynaptic AChRs (red). Regions of overlap between pre- and post-synaptic regions are yellow. WT mice frequently demonstrate poor overlap between synaptic vesicles and AChRs (arrows). NANOG mice showed overlap similar to NMJs from control non-transected limbs. Scale bar = 20 μm. Quantification for percentage of colocalization between synaptic vesicles and AChRs at (**E**) 5 weeks and (**F**) 16 weeks after nerve injury; each point in the dispersion plot represents a single NMJ from n = 6 biological replicates per condition. For 5 weeks dataset: n = 103 NMJs for Control Non-Transected, n = 116 NMJs for WT Transected, n = 95 NMJs for NANOG Transected. For 16 weeks dataset: n = 520 NMJs for Control non-transected, n = 453 NMJs for WT transected, n = 556 NMJs for NANOG transected. All data are presented as Mean ± SEM. Statistical analysis performed using two-way ANOVA with Tukey's multiple comparison test for all graphs. Source data are provided as a Source Data file.

reprogramming of muscle by NANOG can dedifferentiate it to an early-development like state, as seen by increased expression of eMYHC, a protein exclusively expressed during muscle development[94]. Transient NANOG expression also acutely downregulated key genes governing muscle atrophy and increased transcription of genes associated with neurotrophic factor signaling. Neurotropic factors such as BDNF have been shown to play a role in satellite cell proliferation and muscle regeneration[95], as well in maintaining mitochondrial function[96]. BDNF is secreted by both motor neurons and myofibers at the NMJ, and plays a role in postsynaptic maintenance, acetylcholine release, and motor neuron viability[97–99]. The neurotropic factor GDNF is expressed in Soleus and EDL muscles during early myogenesis[100]. Further, the neurotropin receptors p75, TrkA, TrkB, TrkC and Ret are expressed abundantly in the skeletal muscle[101], and cluster around the pre- and post-synaptic sides of the NMJ[102,103]. Hence, we hypothesized that NANOG expression might be priming the muscle to a state that is conducive to innervation.

Indeed, we found that NANOG induced ECM remodeling of the muscle might play a role in improving innervation. Previously, we have shown that NANOG expression restores ECM synthesis in senescent MSCs[104]. Studies on human fetal sclera fibroblasts confirm the role of NANOG in improving Col1 expression[105]. ECM proteins play a crucial role in NMJ formation and synaptogenesis during development. The ECM proteins secreted by each individual myofiber for the synaptic basal lamina mark the location of NMJs and induce synaptic localization[106]. Key ECM proteins that comprise the synaptic cleft include laminin and collagen[107], both of which are upregulated by NANOG. Hence, this ECM remodeling might play a role in creating a permissive environment for axons to grow and form synapses. Enhanced synaptogenesis is confirmed by enhanced colocalization of presynaptic neuronal vesicles, and postsynaptic acetylcholine receptors in NANOG animals. In WT animals, the lack of essential ECM proteins could lead to immature synapses, as evidenced by innervation by multiple axons 5 weeks after injury, many of which might fail to mature over time.

Interestingly, we found that NANOG expression in the muscle had limited effect on molecular markers of muscle fiber atrophy at 5 weeks after nerve injury. This finding is not surprising since multiple studies have demonstrated that expression of atrophy and autophagy associated genes is transient and occurs early during denervation. Specifically, Lifante et al. have reported that Atrogin-1 and Murf proteins involved in muscle proteolysis by the ubiquitin-proteasome system are upregulated within a few days of denervation[108]. Studies by Baumann et al. and Sawano et al. confirm that expression of atrogenes returns to baseline levels within 2 weeks of denervation, playing an important role in early atrophy processes[109,110]. These results indicate that molecular markers of atrophy such as expression of atrogenes and autophagy related proteins change transiently after denervation and assessing expression of these genes 5 weeks post denervation might be too late in the reinnervation process. Several studies in field suggest

that denervation-induced muscle atrophy leads to an increase in mitochondrial reactive oxygen species (ROS) production leading to mitochondrial damage[68–70]. Interestingly, we found that nerve transection in WT animals led to a significant increase in ROS levels that was recovered to levels of non-transected controls in NANOG animals. This finding suggests that changes in mitochondrial metabolism and decreased ROS associated with NANOG expression might play a role in functional outcomes of NANOG-associated improvements in recovery after nerve injury. Most importantly, while molecular markers of atrophy are observed early after denervation, functional changes associated with denervation induced atrophy persist for longer periods of time. Indeed, NANOG expression in the skeletal muscle led to recovery of muscle size and enhanced isometric force production at 5 weeks indicating decreased fiber atrophy.

Most importantly, we show that NANOG expression in the muscle enhances motor function, as evidenced by improved toe-spread reflex, EMG CMAP and muscle force. WT mice show maximum recovery between 5 to 8 weeks after nerve transection but limited improvement thereafter. Interestingly, NANOG expression initiates early recovery after nerve transection. Improvements in toe-spread reflex, EMG CMAP, and maximal force are observed as early as 5 weeks, and recovery continues improving throughout 16 weeks post nerve transection. It is interesting to note that recovery evaluated based on all three parameters- toe-spread, EMG CAMP and synapse formation evidenced by overlap between pre- and post-synaptic regions convey a similar trend in both WT and NANOG mice. While WT mice showed limited improvement in all these parameters after 5 weeks, NANOG mice showed continued improvements throughout 16 weeks post transection. This early recovery and continued improvement in muscle function may be attributed to enhanced transcription of key genes necessary for synaptogenesis. While both WT and NANOG animals upregulated genes associated with NMJ formation and neurogenesis, and downregulated atrophy-related genes, the changes were significantly enhanced by partial reprogramming with NANOG. Though it is difficult to comment on why this might be so, it is very well established that partial reprogramming initiated by embryonic factors (a.k.a. Yamanaka factors) leads to genome-wide epigenetic modifications influencing gene transcription[93,111].

In summary, we clearly demonstrate that NANOG-induced muscle reprogramming can prime adult muscle to accept new synapses and enhance recovery after PNI, without loss of cellular identity. Further studies are needed to decode the exact mechanisms that might be aiding enhanced synaptogenesis. Knowledge of these mechanisms and signaling events that mediate this process is crucial to identify druggable targets and design small molecules that mimic NANOG and can be pharmacologically administered to patients following injury. In this study, NANOG was expressed in the periphery at the time of injury. However, clinical interventions can often only be provided after the injury has taken place. Hence, further work is needed to
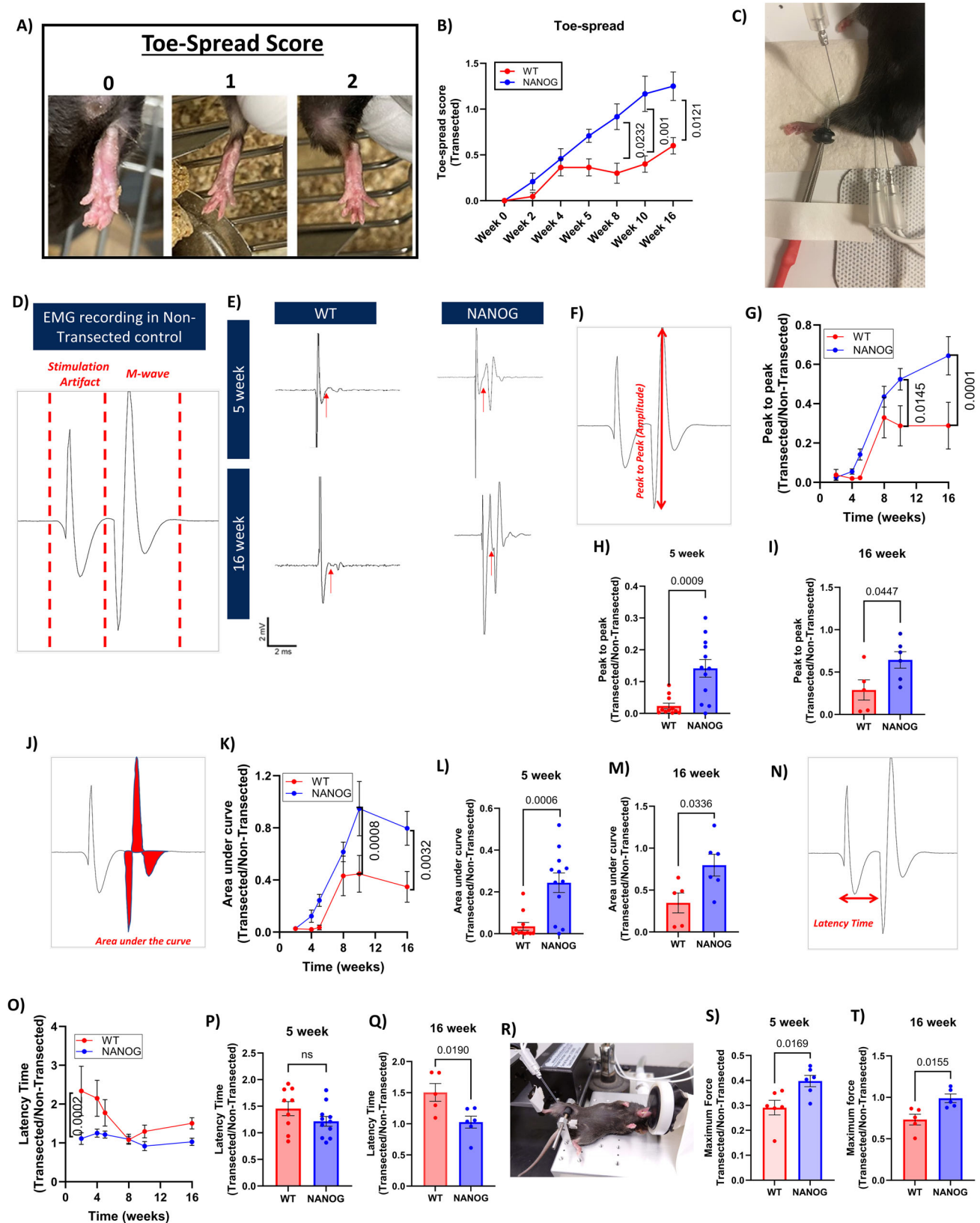
determine the time window after injury wherein NANOG expression leads to functional improvements. Moreover, techniques of reprogramming the muscle can be used in conjunction with nerve conduits, autologous grafts, and stem cells to enhance recovery after PNI. In conclusion, we show for the first time that it is possible to reprogram muscle into an innervation permissive state, leading to enhanced outcomes after nerve injury.

Methods

Generation of ROSA-NANOG transgenic mice

Transgenic mice that express NANOG on exposure to doxycycline (C57BL/6; Col1a1 tetO-Nanog/+; ROSA26rtTA/rtTA) were provided by the laboratory of Dr. Manuel Serrano at The Barcelona Institute of Science and Technology, Spain[112]. The mice carry the M2-rtTA gene inserted within the Rosa26 locus, and a cassette containing NANOG cDNA

Fig. 6 | NANOG mice show enhanced functional recovery after nerve transection. A Depiction of mouse toe spread reflex and assigned scores. **B** Quantification of toe-spread reflex from Week 0-16 after nerve transection; for weeks 0-5: WT-$n = 11$, NANOG- n = 12 biological replicates; for weeks 8-16: WT- $n = 5$, NANOG-$n = 6$ biological replicates. **C** Setup for needle EMG recordings. **D** A typical EMG waveform recorded in non-transected control mice. **E** Representative waveforms from WT and NANOG transected limbs at 5-and 16- weeks after injury. The start of M-wave is marked by red arrows. **F** Schematic depicting the amplitude of the CMAP M-wave. **G** Quantification of normalized EMG amplitude from weeks 0-16 after nerve transection in WT and NANOG mice. **H** EMG amplitude at 5 weeks and (**I**) 16 weeks post nerve injury. **J** Schematic depicting the area of an M-wave. **K** Quantification of normalized EMG area from weeks 0-16 after nerve transection in WT and NANOG mice. **L** CMAP M-wave area at 5 weeks and (**M**) 16 weeks post nerve

injury. **N** Schematic of latency time. **O** Quantification of normalized EMG latency time from weeks 0-16 after nerve transection in WT and NANOG mice. **P** Latency time at 5 weeks and (**Q**) 16 weeks post nerve injury; In graphs **G–Q**, for weeks 0-5: WT- $n = 11$, NANOG- $n = 12$ biological replicates; for weeks 8-16: WT-$n = 5$, NANOG-$n = 6$ biological replicates. **R** Setup for muscle force measurement in live mice using the Aurora force transducer. Maximum force recorded at stimulation frequency of 150 Hz from both transectedand non-transected limbs at (**S**) 5 weeks and (**T**) 16 weeks. Force in the transected side was normalized to the average force of the control non-transected limb; For both WT and NANOG, $n = 6$ biological replicates at 5 weeks (**S**). and $n = 5$ biological replicates at 16 weeks (**T**). For **B, G, K** and **L**, statistics performed using two-way ANOVA with Sidak's test. For **H, I, L, M, P, Q, S**, and **T**, statistics performed using unpaired t-test. All data are presented as Mean ± SEM. Source data are provided as a Source Data file.

under the Dox-responsive promoter (tetO) is inserted downstream of the Col1a1 locus. Mice were bred and genotyped using polymerase chain reaction (PCR) of tail DNA using the primers in Supplementary Table 1 for DNA amplification. Wild-type (WT) mice that did not express NANOG served as controls. Experiments were performed with equal number of male and female mice (WT: 5 females and 6 males; NANOG: 5 females and 6 males) that were 3-4 months old at the time of transection. The mice were kept in a controlled environment where they experienced a 12-hour cycle of light and darkness from 6:00 to 18:00. The room temperature was maintained at 22 °C, and they had unrestricted access to food and water. The humidity levels were maintained between 30% and 70%. All research involving animals followed approved protocols from the Institutional Animal Care and Use Committee (IACUC) of the University at Buffalo. These protocols adhered to the Animal Welfare Act, Public Health Service Policy on humane care and use of laboratory animals, and other relevant federal statutes and regulations governing animal experimentation.

Elvax preparation and implantation
For slow release of doxycycline (Dox), Elvax sheets were prepared as previously described[35]. Briefly, Elvax 40 W beads (obtained as a gift from DuPont) were subjected to 3-4 rounds of washing in 95% ethanol with continuous stirring over the course of one week. Subsequently, they were dried using filter paper. In a glass culture tube, 100 mg of these beads were dissolved in 900 µl of methylene chloride. For drug incorporation, Dox (25 mg/100 µl; Catalog # D9891, Sigma-Aldrich, St. Louis, MO), or saline was dissolved in a solution of 1% fast green in DMSO. The Elvax mixture was then vortexed at a medium speed for 3 minutes and poured onto a glass slide with a cut piece of Parafilm serving as a spacer. The slide, along with a second slide clamped on top, was placed on powdered dry ice. The Elvax was then exposed to a temperature of 70° for 2-5 days before being shifted to 20 °C. Before use, the Elvax was briefly rehydrated using saline.

To implant the Elvax, 9-10 months old mice were anesthetized using isoflurane. An incision was made in the lateral skin of the distal hindlimb, and the fascial plane between the anterior and posterior compartments was cut. Two rectangular pieces of Elvax measuring 3 × 4 mm were placed in the hindlimb. One was placed subcutaneously over the (TA) muscle. The second was placed between the anterior and posterior compartments near the gastrocnemius and soleus muscles (Fig. 1A, B). After suturing the incision, the mice were returned to their cages following a warming period. The right leg received Elvax impregnated with Dox-Elvax, while the left leg did not receive any Elvax. The Elvax was left in place for 2 weeks and removed thereafter in a second surgery. In some control experiments the right leg was implanted with Dox-Elvax and the left leg with DMSO-Elvax to verify that Elvax placement did not damage the muscle directly.

Nerve transection
Mice were anesthetized using isoflurane. The right sciatic nerve for each animal was completely transected 3 mm proximal to the

trifurcation and immediately repaired with 10-0 micro suture (Polypropylene-Sharpoint, eSutures.com). Dox-Elvax was implanted on the right hindlimb to both ROSA-NANOG and WT mice in the same surgery. Surgery was conducted in 6 male and 5 female WT mice, and 6 male and 5 female NANOG mice. These mice were 3-4 months old at the time of nerve transection. Recovery was monitored over several weeks, and toe-spread reflex and EMG were recorded at 2, 4, 5, 8, 10 and 16 weeks after nerve transection. After 5 weeks of nerve injury, 6 mice from each condition (WT: $n = 3$ males and $n = 3$ females; NANOG: $n = 4$ males and $n = 2$ females) were euthanized, and muscle and nerve samples were collected for analysis. After 16 weeks, the remaining mice were euthanized, and tissues were collected for analysis. We chose to focus on 2, 4, 5, 8, 10 and 16 weeks timepoints based upon previously published work from the Woolf and Snyder-Warwick labs that follow recovery up to 16 weeks after sciatic nerve transection with microsuture repair[25,76]. Initial reinnervation occurs between 4 and 8 weeks in this model, and hence we focused our EMG and behavioral measurements on these timepoints. RNA-Seq has previously been used to follow changes in gene expression up to 8 weeks after sciatic nerve injury[113]. To understand early transcription changes, we performed RNA sequencing at 5 weeks post sciatic nerve transection. Further, to evaluate if these changes in transcription persist over a longer period, we also performed RNA seq at the final time-point of 16 weeks post nerve transection.

Toe-spread test
The toe-spread reflex test was conducted as described previously[34]. The mice were carefully covered with a cloth and lifted by their tail, allowing their hind leg digits to fully extend and spread. The reflex response was evaluated and scored as follows: 0 indicated no spreading of the toes, 1 represented intermediate spreading, and 2 indicated complete spreading (refer to Fig. 6A). The test was conducted at Weeks 0, 2,4,5,8,10, and 16 weeks.

EMG recordings
Mice were anesthetized by isoflurane. EMG recordings were made using procedures modified from Arnold et al. [114]. The sciatic nerve was stimulated at the proximal hind limb above the site of transection using two 28 G monopolar electrodes (DTM Series, Electrode Store). Stimulation was provided by a Grass S88 (Quincy, MA) using square-wave pulses of 0.1 ms duration and intensity ranging from 1-10 mA. Recordings were made using one fine ring electrode (reference) placed around the ankle and a second 28 G monopolar electrode (active) placed mid-belly in the TA. A ground electrode was placed around the tail to allow for differential amplification of the CMAP waveform (BDA-H-4, WPI, Inc). Signals were acquired digitally and analyzed using Spike2 software (CED, Inc, Cambridge, UK). Stimulation intensity was increased until there was no more increase in CMAP amplitude. To ensure supramaximal stimulation, stimulation intensity was increased to ~120% of maximal response. EMG recordings were made from both the left control non-denervated TA and on the side of transection

(right). EMG CMAP results are presented as ratio of the recordings from left and right sides.

Protein isolation and western blot

TA muscles were weighed, and 9-10 mg of the muscle was cut for protein isolation. Muscles were lysed in RIPA buffer (Catalog # 89900, Thermo Fisher Scientific, Waltham, MA) containing 1X Halt protease and phosphatase inhibitor (Catalog # 78442, Thermo Fisher Scientific). TA muscle tissues were homogenized by bead disruption using Bead Lysis tubes (Catalog # GREENR5-RNA, Next Advance, Troy, NY) using Bullet Blender (Stellar Scientific, Baltimore, MD), which was chilled using dry-ice. Lysates were centrifuged and 1X Blue loading dye (Cell Signaling, Danvers, MA) and 1X DTT reducing agent (Cell Signaling) were added. Protein was denatured by incubation at 95 °C for 5 min and proteins were loaded at 45 μg per lane and were separated in 10% acrylamide gels (Thermo Fisher Scientific) by SDS-polyacrylamide gel electrophoresis based on their molecular weight. After transferring proteins to nitrocellulose membranes (Bio-Rad, Hercules, California) using the Trans-Blot Turbo Transfer System (Bio-Rad), the membranes were blocked in 5% (w/v) non-fat dry milk in blocking buffer for 1 h at room temperature. Subsequently, membranes were incubated over-night at 4 °C with antibodies listed in Supplementary Table 2. Membranes were incubated for 1 h at room temperature with Anti-rabbit IgG HRP linked (Catalog # 7074, Cell Signaling). Finally, the protein bands were visualized using horseradish peroxidase-conjugated secondary antibodies and a chemiluminescence kit (Cell Signalling) according to the manufacturer's instructions. Luminescent blots were imaged using ChemiDoc™ Touch Imaging System (Bio-Rad).

RNA isolation from tissues and qPCR

TA muscles were weighed, and 9-10 mg of the muscle was cut for RNA isolation. RNA was isolated using RNeasy Fibrous Tissue Mini Kit (Catalog # 74704, Qiagen, Valencia, CA) as per manufacturer's instructions. cDNA was synthesized using the Superscript III cDNA Synthesis Kit (Thermo Fisher Scientific). For real-time PCR analysis, 1 μg of cDNA was used per reaction, and the SYBR Green Kit (Bio-Rad) was employed. The specific primers for the real-time PCR were listed in Supplementary Table 3. The qPCR cycle determination was performed using Bio-Rad Software CFX Manager Ver 3.1.

Whole mount immunocytochemistry

The soleus and EDL muscles were placed in a dish coated with Sylgard and soaked in saline solution. Connective tissue was removed from the muscles, and they were fixed by immersing them in 4% paraformaldehyde solution at pH 7.4 for 15 minutes. Subsequently, the muscles were transferred to microcentrifuge tubes and washed three times with PBS. They were then exposed to rhodamine-conjugated-α-bungarotoxin (α-BTX; Catalog # T1175, Life Technologies, Grand Island, NY) at a concentration of 10% for 20 minutes, followed by three additional rinses with PBS. To permeabilize the tissue, the muscles were immersed in −20 °C methanol for 5 minutes and then rinsed three times with PBS.

Next, the muscles were blocked in a solution containing 2% bovine serum albumin, 0.1% sodium azide, and 0.2% Triton-X100 in saline for 60 minutes. They were then incubated overnight at room temperature with primary antibodies against SV2 (synaptic vesicles) and 2H3 (neurofilament) (Supplementary Table 2). The staining was visualized using a secondary antibody, Alexa Fluor 488 donkey anti-mouse (RRID: AB_2556542, Catalog # R37114; Life Technologies). Finally, the muscles were filleted into two halves and pressed flat on the slide via coverslip and Vectashield mounting medium. Staining was observed using conventional epifluorescence microscopy (63× oil objective, BX51; Olympus) and confocal microscopy (63× oil objective, LSM 510 Meta NLO; Zeiss). NMJ morphology, including the extent of colocalization between synaptic vesicles and acetylcholine receptors was assessed using the publicly available NMJ-morph tool in Fiji (ImageJ).

Tissue embedding and immunostaining

TA, EDL and Soleus muscles were isolated, and connective tissue, if any, was carefully removed. The muscle was gently dried and then immersed in OCT embedding medium (Sakura Finetek, Torrance, CA). Next the tissues were transferred to a container containing dry ice and 2-Methylbutane (Sigma-Aldrich) to freeze the tissues. For staining, tissue sections were cut to 10 μm thickness using a cryostat (Leica CM1950, Buffalo Grove, IL) at −20 °C, and placed on positively charged glass slides (Stellar Scientific). Sections were stored at −80 °C.

For immunostaining for eMYHC, Pax7 and Laminin, tissues were prepared by first washing them three times in PBS to remove the OCT embedding medium. Subsequently, they were fixed at room temperature, using 4% paraformaldehyde for 10 minutes. The slides were washed thrice. Next, they were immersed in R-Buffer A (Electron Microscopy Sciences, Hatfield, PA) for antigen retrieval, with the temperature raised to 95 °C for 20 minutes, followed by gradual cooling. To quench endogenous peroxidase activity, the slides were treated with Tyramide H2O2 solution (Alexa Fluor™ 555 Tyramide SuperBoost™ Kit, Thermo Fisher Scientific) for 30 minutes. This was followed by blocking with a mixture of 5% (w/v) goat serum and 5% (w/v) BSA in PBS for 1 hour, followed by Tyramide Blocking Buffer for another hour, and mouse IgG blocking reagent (MOM, Vectors Lab, Burlingame, CA) for an additional hour, following the manufacturer's protocol. The tissue sections were then incubated overnight at 4 °C with primary antibodies (Supplementary Table 2) diluted in MOM diluent. The next day, the samples were washed thrice with PBS and stained using the Tyramide kit goat anti-mouse secondary antibody, according to the Tyramide kit protocol. Finally, the samples were stained with Alexa Fluor 568, 488, or 647 conjugated goat anti-rabbit or goat anti-mouse secondary antibodies for 1 hour at room temperature. Finally, the cells were stained with Hoechst 33342 nuclear dye (1:1000 dilution in PBS, Thermo Fisher Scientific) for 5 min at RT, followed by three washes in PBS. The slides were coverslipped using ProLong™ Diamond Antifade Mountant (Thermo Fisher Scientific).

For immunostaining for SV2, 2H3 and ACHRs, slides were washed and fixed as described previously[34]. They were then blocked in a solution containing 2% bovine serum albumin, 0.1% sodium azide, and 0.2% Triton-X100 in saline for 60 minutes at room temperature. This was followed by incubation with primary antibodies for SV2 and 2H3 for 60 minutes at room temperature. The slides were then washed thrice and incubated with α-BTX at a concentration of 10% for 20 minutes, followed by three additional rinses with PBS. Finally, the slides were stained with Hoechst 33342, washed with PBS thrice, and mounted for imaging.

For IgG uptake assay, the TA muscle sections were fixed at room temperature using 4% paraformaldehyde for 10 minutes. The slides were washed thrice. This was followed by blocking with a mixture of 5% (w/v) goat serum and 5% (w/v) BSA in PBS for 1 hour, followed by incubating with Laminin antibody for 1 hr at room temperature. The slides were washed thrice. Next, samples were incubated with Alexa Fluor 488 conjugated goat anti-rabbit secondary antibody to label laminin, and co-labeling myofibers with mouse anti-IgG Alexa Fluor 564 secondary antibody for 1 hour at room temperature. Finally, the cells were stained with Hoechst 33342 nuclear dye (1:1000 dilution in PBS, Thermo Fisher Scientific) for 5 min at RT, followed by three washes in PBS. The slides were coverslipped using ProLong™ Diamond Antifade Mountant (Thermo Fisher Scientific).

ROS measurement in muscle tissue

For detection of ROS in muscle tissue sections, 10 mg of GA was homogenized in 300 μL mammalian cell lysis buffer (ab179835, Abcam) by bead disruption in bead lysis tubes using the Bullet Blender® Gold tissue homogenizer. Protein concentration of samples was determined using BCA protein assay kit. Total free radical presence in 5 μg of each sample was measured using the DCF ROS/RNS Assay Kit (Cat # ab238535, Abcam) as per manufacturer recommended protocol.

RNA sequencing and pathway analysis

The global gene expression profiles were characterized by next generation RNA sequencing using Illumina platform. To this end, total RNA was isolated for all conditions using RNeasy Mini Kit and quality control analysis was performed by RNA gel and Agilent Fragment Analyzer. Sequencing libraries were prepared as per standard Illumina protocols (Illumina Stranded Total RNA Prep with Ribo-Zero Plus), quality checked, and quantified by Kapa Biosystems qPCR. The multiplexed libraries were sequenced in pair-end (2 × 50 bp) on the NovaSeq 6000 at 300 pM with 1% loading control.

Sequencing reads passed quality filter from Illumina RTA were first processed using FASTQC (v0.10.1) for sequencing base quality control. Then sample reads were aligned to the human reference genome (GRCm38) and GENCODE (version 22) annotation database using STAR2[115]. Second round of QC using RSeQC[116] was applied to mapped bam files to identify potential RNASeq library preparation problem. Gene level raw counts were obtained using Subread[117] package. Differential gene expression analysis was performed using DESeq2[118] and pathway analysis was performed with the Gene Set Enrichment Analysis (GSEA) method (4.2)[119], and the Gene ontology Resource[120,121]. The GSEA tool was chosen to run the analysis using the normalized gene count data that pre-filtered the low count genes. Pathway analysis was run against MSigDB, a collection of annotated and curated gene set repositories offered by the developer of GSEA (Broad Institute MIT and Harvard). This particular run used C2 of version 7.5 collection, containing 2318 gene sets from various well-known and up-to-date pathway databases such as BioCarta, KEGG and Reactome among others.

In-vivo muscle isometric force measurement

Muscle isometric force was measured in live animals as described previously [32]. In short, mice were anesthetized using isoflurane. Next, the skin above the TA was carefully shaved, and the mice were placed on a heated stage maintained at 37 °C by circulating warm water. The knee of the mice was clamped using a knee clamp attached to the stage, and the leg was secured onto a footplate connected to a servomotor (1300 A: 3-in-1 Whole Animal System−Mouse; Aurora Scientific, CA). Two 28 G monopolar needle electrodes were inserted subcutaneously medial and lateral to the TA muscle. The optimal position for muscle contraction was determined by adjusting the distance between the footplate and knee and stimulating the muscle with a single electrical pulse (25 mA, 0.2 ms pulse width; previously optimized conditions). Once the muscle force ceased to increase, the position was considered the best for muscle contraction. Subsequently, Tetanic force was measured by stimulating the muscle with a 500 ms duration and 0.2 ms pulse width at frequencies ranging from 10 to 200 Hz (10, 20, 35, 50, 65, 80, 100, 150, 200 Hz), with a 2-minute interval between each stimulation. At the end of the experiments, the mice were returned to their cages with a warming pad and monitored until they regained consciousness and exhibited normal behavior. The data obtained were analyzed using 611 A Dynamic Muscle Analysis (DMA) software. Maximum Force was recorded at the stimulation frequency of 150 Hz and plotted as such.

Nerve labeling

The methodology was based on previously published protocol[122]. Briefly, nerves were isolated at 5 weeks and 16 weeks after PNI. The nerve was placed into Trump's fixative for 24 hr, followed by 24 hr in 4% glutaraldehyde. Samples were embedded in Tissue-Tek® O.C.T. Compound and frozen at −20 °C and long-term storage at −80 °C. Tissue was cut at 10 μm thickness using a cryostat and stained with FluoroMyelin™ Red (Catalog # F34652; Thermo Fisher Scientific), and sections were placed on treated glass slides (Catalog # 9951LPLUS; Thermo Fisher Scientific). Nerves were imaged over ECLIPSE Ti2 Series

NIKON Inverted Microscope. Main grey intensity, which reflected the quantity of myelination in the nerve, was quantified by individuals blinded to experimental conditions.

Imaging and image analysis

The Zeiss Axio Observer Z1 inverted microscope (LSM 510; Zeiss, Oberkochen, Germany) equipped with an ORCA-ER CCD camera (Hamamatsu, Japan) was used to acquire immunocytochemistry and immunohistochemistry images. Confocal images were acquired using the Stellaris 5 confocal microscope (Leica).

Image analysis was performed using Fiji (ImageJ). For analyzing colocalization between synaptic vesicles and acetylcholine receptors, the colocalization threshold tool was used. Area of interest was selected over the staining for α-BTX, after normalizing by subtracting fluorescence intensity in the region of interest over the AChRs from fluorescence intensity in adjacent control areas of the same size. Percentage of overlap of selected region of interest (ROI) in α-BTX channel with SV2 channel was plotted. To analyze fiber size, each muscle fiber was manually selected, and area was measured. To analyze number of fibers positive for eMYHC, positively stained fibers were manually counted. To quantify the number of Pax7+ nuclei, all nuclei that co-stained for Pax7 and Hoechst 33342 (DAPI) were manually counted.

Statistical analysis

All data was organized and collected as Microsoft Excel spreadsheet and statistical analysis was performed using GraphPad Prism®8 Software. Comparisons among multiple groups and time-points were performed using two-way ANOVA followed by Tukey's post hoc test, Sidak's multiple comparisons test, or Uncorrected Fisher's LSD test. Comparisons among more than two samples were performed using one-way ANOVA followed by Tukey's post hoc test. Unpaired t-tests were used to compare data depicting only two conditions. Comparisons having p-value < 0.05 was considered statistically significant. All data was plotted as Mean ± SEM.

Reporting summary

Further information on research design is available in the Nature Portfolio Reporting Summary linked to this article.

Data availability

All data generated in this study are provided in the Supplementary Information/Source Data files. Source data have been deposited in Figshare and can be accessed using the link https://doi.org/10.6084/m9.figshare.26300842. The RNA-seq data discussed in this publication are accessible through Sequence Read Archive (SRA) Series accession number PRJNA1160713.

References

1. Taylor, C. A., Braza, D., Rice, J. B. & Dillingham, T. The incidence of peripheral nerve injury in extremity trauma. *Am. J. Phys. Med. Rehab.* **87**, 381–385 (2008).
2. Rivera, J. C., Glebus, G. & Cho, M. Disability following combat-sustained nerve injury of the upper limb. *bone Jt. J.* **96**, 254–258 (2014).
3. Bergmeister, K. D. et al. Acute and long-term costs of 268 peripheral nerve injuries in the upper extremity. *PloS one* **15**, e0229530 (2020).
4. Grinsell, D. & Keating, C. Peripheral nerve reconstruction after injury: a review of clinical and experimental therapies. *BioMed. Res. Int.* **2014**, 698256 (2014).
5. Padovano, W. M. et al. Incidence of nerve injury after extremity trauma in the United States. *Hand* **17**, 615–623 (2022).

6. Conway, P. H. Factors associated with increased US health care spending: implications for controlling health care costs. *Jama* **318**, 1657–1658 (2017).

7. Rbia, N. & Shin, A. Y. The role of nerve graft substitutes in motor and mixed motor/sensory peripheral nerve injuries. *J. Hand Surg.* **42**, 367–377 (2017).

8. Liu, W. et al. Allotransplanted neurons used to repair peripheral nerve injury do not elicit overt immunogenicity. *PLoS One* **7**, e31675 (2012).

9. Kehoe, S., Zhang, X. & Boyd, D. FDA approved guidance conduits and wraps for peripheral nerve injury: a review of materials and efficacy. *Injury* **43**, 553–572 (2012).

10. Wangensteen, K. J. & Kalliainen, L. K. Collagen tube conduits in peripheral nerve repair: a retrospective analysis. *Hand* **5**, 273–277 (2010).

11. Haastert-Talini, K. et al. Chitosan tubes of varying degrees of acetylation for bridging peripheral nerve defects. *Biomaterials* **34**, 9886–9904 (2013).

12. Marcol, W. et al. Reduction of post-traumatic neuroma and epineural scar formation in rat sciatic nerve by application of microcrystallic chitosan. *Microsurgery* **31**, 642–649 (2011).

13. Navissano, M., Malan, F., Carnino, R. & Battiston, B. Neurotube® for facial nerve repair. *Microsurgery* **25**, 268–271 (2005).

14. Den Dunnen, W. et al. Poly (DL-lactide-ε-caprolactone) nerve guides perform better than autologous nerve grafts. *Microsurgery: Off. J. Int. Microsurgical Soc. Eur. Federation Societies Microsurgery* **17**, 348–357 (1996).

15. Kaplan, H. M., Mishra, P. & Kohn, J. The overwhelming use of rat models in nerve regeneration research may compromise designs of nerve guidance conduits for humans. *J. Mater. Sci.: Mater. Med.* **26**, 1–5 (2015).

16. Kornfeld, T., Vogt, P. M. & Radtke, C. Nerve grafting for peripheral nerve injuries with extended defect sizes. *Wien. Medizinische Wochenschr. (1946)* **169**, 240 (2019).

17. Saheb-Al-Zamani, M. et al. Limited regeneration in long acellular nerve allografts is associated with increased Schwann cell senescence. *Exp. Neurol.* **247**, 165–177 (2013).

18. Patel, N. P., Lyon, K. A. & Huang, J. H. An update–tissue engineered nerve grafts for the repair of peripheral nerve injuries. *Neural Regeneration Res.* **13**, 764 (2018).

19. Fathi, S. S. & Zaminy, A. Stem cell therapy for nerve injury. *World J. Stem Cells* **9**, 144 (2017).

20. Yi, S. et al. Application of stem cells in peripheral nerve regeneration. *Burns Trauma* **8**, tkaa002 (2020).

21. Liu, M., Li, K., Wang, Y., Zhao, G. & Jiang, J. Stem cells in the treatment of neuropathic pain: research progress of mechanism. *Stem Cells Intern.* **2020**, 8861251 (2020).

22. Höke, A. A (heat) shock to the system promotes peripheral nerve regeneration. *J. Clin. Investig.* **121**, 4231–4234 (2011).

23. Kostrominova, T. Y. Vol. 23 7489 (MDPI, 2022).

24. Tang, H. et al. A histone deacetylase 4/myogenin positive feedback loop coordinates denervation-dependent gene induction and suppression. *Mol. Biol. Cell* **20**, 1120–1131 (2009).

25. Sakuma, M. et al. Lack of motor recovery after prolonged denervation of the neuromuscular junction is not due to regenerative failure. *Eur. J. Neurosci.* **43**, 451–462 (2016).

26. de Lázaro, I., Cossu, G. & Kostarelos, K. Transient transcription factor (OSKM) expression is key towards clinical translation of in vivo cell reprogramming. *EMBO Mol. Med.* **9**, 733–736 (2017).

27. Ocampo, A. et al. In vivo amelioration of age-associated hallmarks by partial reprogramming. *Cell* **167**, 1719–1733.e1712 (2016).

28. de Lázaro, I. et al. Non-viral, tumor-free induction of transient cell reprogramming in mouse skeletal muscle to enhance tissue regeneration. *Mol. Ther.* **27**, 59–75 (2019).

29. Han, J. et al. Nanog reverses the effects of organismal aging on mesenchymal stem cell proliferation and myogenic differentiation potential. *Stem Cells* **30**, 2746–2759 (2012).

30. Rong, N. et al. Restoring extracellular matrix synthesis in senescent stem cells. *FASEB J.* **33**, 10954 (2019).

31. Shahini, A. et al. NANOG restores the impaired myogenic differentiation potential of skeletal myoblasts after multiple population doublings. *Stem Cell Res.* **26**, 55–66 (2018).

32. Shahini, A. et al. Ameliorating the hallmarks of cellular senescence in skeletal muscle myogenic progenitors in vitro and in vivo. *Sci. Adv.* **7**, eabe5671 (2021).

33. Rajabian, N. et al. Methionine adenosyltransferase2A inhibition restores metabolism to improve regenerative capacity and strength of aged skeletal muscle. *Nat. Commun.* **14**, 886 (2023).

34. Personius, K. E., Siebert, D., Koch, D. W. & Udin, S. B. Blockage of neuromuscular glutamate receptors impairs reinnervation following nerve crush in adult mice. *Front. Cell. Neurosci.* **16**, 1000218 (2022).

35. Personius, K. E., Slusher, B. S. & Udin, S. B. Neuromuscular NMDA receptors modulate developmental synapse elimination. *J. Neurosci.* **36**, 8783–8789 (2016).

36. Chen, B., You, W., Wang, Y. & Shan, T. The regulatory role of Myomaker and Myomixer–Myomerger–Minion in muscle development and regeneration. *Cell. Mol. Life Sci.* **77**, 1551–1569 (2020).

37. Bi, P. et al. Fusogenic micropeptide Myomixer is essential for satellite cell fusion and muscle regeneration. *Proc. Natl Acad. Sci.* **115**, 3864–3869 (2018).

38. Lee, K.-H. et al. Bidirectional signaling of neuregulin-2 mediates formation of GABAergic synapses and maturation of glutamatergic synapses in newborn granule cells of postnatal hippocampus. *J. Neurosci.* **35**, 16479–16493 (2015).

39. Ponomareva, O. et al. Stimulation of acetylcholine receptor transcription by neuregulin-2 requires an N-box response element and is regulated by alternative splicing. *Neuroscience* **134**, 495–503 (2005).

40. Robinson, K. G. et al. Neuromotor synapses in Escobar syndrome. *Am. J. Med. Genet. Part A* **161**, 3042–3048 (2013).

41. Strelau, J. et al. Progressive postnatal motoneuron loss in mice lacking GDF-15. *J. Neurosci.* **29**, 13640–13648 (2009).

42. Jiang, W.-W. et al. Emerging roles of growth differentiation factor-15 in brain disorders. *Exp. Therapeutic Med.* **22**, 1–11 (2021).

43. Demyanenko, G. P. et al. Neural cell adhesion molecule NrCAM regulates Semaphorin 3F-induced dendritic spine remodeling. *J. Neurosci.* **34**, 11274–11287 (2014).

44. Wang, Y., Lin, L., Lai, H., Parada, L. F. & Lei, L. Transcription factor Sox11 is essential for both embryonic and adult neurogenesis. *Developmental Dyn.* **242**, 638–653 (2013).

45. Hitachi, K., Nakatani, M. & Tsuchida, K. Long non-coding RNA myoparr regulates GDF5 expression in denervated mouse skeletal muscle. *Non-Coding RNA* **5**, 33 (2019).

46. Wood, S., Pritchard, J. & Sofroniew, M. Re-expression of nerve growth factor receptor after axonal injury recapitulates a developmental event in motor neurons: differential regulation when regeneration is allowed or prevented. *Eur. J. Neurosci.* **2**, 650–657 (1990).

47. Deng, S. et al. Plexin-B2, but not Plexin-B1, critically modulates neuronal migration and patterning of the developing nervous system in vivo. *J. Neurosci.* **27**, 6333–6347 (2007).

48. Liu, S. et al. Overexpression of bone morphogenetic protein 7 reduces oligodendrocytes loss and promotes functional recovery after spinal cord injury. *J. Cell. Mol. Med.* **25**, 8764–8774 (2021).

49. Kwon, Y. K. et al. Activation of ErbB2 during wallerian degeneration of sciatic nerve. *J. Neurosci.* **17**, 8293–8299 (1997).

50. Winbanks, C. E. et al. The bone morphogenetic protein axis is a positive regulator of skeletal muscle mass. *J. Cell Biol.* **203**, 345–357 (2013).

51. Sugg, K. B., Korn, M. A., Sarver, D. C., Markworth, J. F. & Mendias, C. L. Inhibition of platelet-derived growth factor signaling prevents muscle fiber growth during skeletal muscle hypertrophy. *FEBS Lett.* **591**, 801–809 (2017).

52. von Maltzahn, J., Chang, N. C., Bentzinger, C. F. & Rudnicki, M. A. Wnt signaling in myogenesis. *Trends cell biol.* **22**, 602–609 (2012).

53. Yamamoto, M. et al. Loss of MyoD and Myf5 in skeletal muscle stem cells results in altered myogenic programming and failed regeneration. *Stem Cell Rep.* **10**, 956–969 (2018).

54. Misgeld, T., Kummer, T. T., Lichtman, J. W. & Sanes, J. R. Agrin promotes synaptic differentiation by counteracting an inhibitory effect of neurotransmitter. *Proc. Natl Acad. Sci.* **102**, 11088–11093 (2005).

55. Samuel, M. A., Valdez, G., Tapia, J. C., Lichtman, J. W. & Sanes, J. R. Agrin and synaptic laminin are required to maintain adult neuromuscular junctions. *PLoS One* **7**, e46663 (2012).

56. Ksiazek, I. et al. Synapse loss in cortex of agrin-deficient mice after genetic rescue of perinatal death. *J. Neurosci.* **27**, 7183–7195 (2007).

57. Wu, M. et al. Impairment of inhibitory synapse formation and motor behavior in mice lacking the NL2 binding partner LHFPL4/GARLH4. *Cell Rep.* **23**, 1691–1705 (2018).

58. Qi, Y. et al. Identification of chloride channels CLCN3 and CLCN5 mediating the excitatory Cl– currents activated by sphingosine-1-phosphate in sensory neurons. *Front. Mol. Neurosci.* **11**, 33 (2018).

59. Dunn, A. R. et al. Synaptic vesicle glycoprotein 2C (SV2C) modulates dopamine release and is disrupted in Parkinson disease. *Proc. Natl Acad. Sci.* **114**, E2253–E2262 (2017).

60. Nagatsu, T. et al. The role of tyrosine hydroxylase as a key player in neuromelanin synthesis and the association of neuromelanin with Parkinson's disease. *J. Neural Transm.* **130**, 611–625 (2023).

61. Yamazaki, T. et al. Activation of MAP kinases, Akt and PDGF receptors in injured peripheral nerves. *J. Peripheral Nerv. Syst.* **14**, 165–176 (2009).

62. Funa, K. & Sasahara, M. The roles of PDGF in development and during neurogenesis in the normal and diseased nervous system. *J. Neuroimmune Pharmacol.* **9**, 168–181 (2014).

63. Koropouli, E. & Kolodkin, A. L. Semaphorins and the dynamic regulation of synapse assembly, refinement, and function. *Curr. Opin. Neurobiol.* **27**, 1–7 (2014).

64. Attaix, D. et al. The ubiquitin–proteasome system and skeletal muscle wasting. *Essays Biochem.* **41**, 173–186 (2005).

65. Mitch, W. E. & Goldberg, A. L. Mechanisms of muscle wasting—the role of the ubiquitin–proteasome pathway. *N. Engl. J. Med.* **335**, 1897–1905 (1996).

66. Sandri, M. Autophagy in health and disease. 3. Involvement of autophagy in muscle atrophy. *Am. J. Physiol.-Cell Physiol.* **298**, C1291–C1297 (2010).

67. Bodine, S. C. et al. Akt/mTOR pathway is a crucial regulator of skeletal muscle hypertrophy and can prevent muscle atrophy in vivo. *Nat. Cell Biol.* **3**, 1014–1019 (2001).

68. Muller, F. L. et al. Denervation-induced skeletal muscle atrophy is associated with increased mitochondrial ROS production. *Am. J. Physiol.-Regulatory, Integr. Comp. Physiol.* **293**, R1159–R1168 (2007).

69. Scalabrin, M. et al. Redox responses in skeletal muscle following denervation. *Redox Biol.* **26**, 101294 (2019).

70. Yang, X. et al. Denervation drives skeletal muscle atrophy and induces mitochondrial dysfunction, mitophagy and apoptosis via miR-142a-5p/MFN1 axis. *Theranostics* **10**, 1415 (2020).

71. Zhang, W., Liu, Y. & Zhang, H. Extracellular matrix: An important regulator of cell functions and skeletal muscle development. *Cell Biosci.* **11**, 1–13 (2021).

72. Washbourne, P. et al. Cell adhesion molecules in synapse formation. *J. Neurosci.* **24**, 9244–9249 (2004).

73. Turney, S. G. & Lichtman, J. W. Reversing the outcome of synapse elimination at developing neuromuscular junctions in vivo: evidence for synaptic competition and its mechanism. *PLoS Biol.* **10**, e1001352 (2012).

74. Jones, R. A. et al. NMJ-morph reveals principal components of synaptic morphology influencing structure–function relationships at the neuromuscular junction. *Open Biol.* **6**, 160240 (2016).

75. Personius, K. E. & Sawyer, R. P. Terminal Schwann cell structure is altered in diaphragm of mdx mice. *Muscle Nerve* **32**, 656–663 (2005).

76. Vannucci, B. et al. What is Normal? Neuromuscular junction reinnervation after nerve injury. *Muscle Nerve* **60**, 604–612 (2019).

77. Bozkurt, A. et al. Aspects of static and dynamic motor function in peripheral nerve regeneration: SSI and CatWalk gait analysis. *Behavioural Brain Res.* **219**, 55–62 (2011).

78. Ma, C. H. E. et al. Accelerating axonal growth promotes motor recovery after peripheral nerve injury in mice. *J. Clin. Investig.* **121** (2011).

79. Mills, K. R. The basics of electromyography. *J. Neurol., Neurosurg. Psychiatry* **76**, ii32–ii35 (2005).

80. Kouzaki, K., Nosaka, K., Ochi, E. & Nakazato, K. Increases in M-wave latency of biceps brachii after elbow flexor eccentric contractions in women. *Eur. J. Appl. Physiol.* **116**, 939–946 (2016).

81. Aman, M. et al. Peripheral nerve injuries in children—prevalence, mechanisms and concomitant injuries: a major trauma center's experience. *Eur. J. Med. Res.* **28**, 1–7 (2023).

82. Birch, R. & Achan, P. Peripheral nerve repairs and their results in children. *Hand Clin.* **16**, 579–595 (2000).

83. Boecker, A. H. et al. Evaluation of MR-neurography in diagnosis and treatment in peripheral nerve surgery of the upper extremity: A matched cohort study. *Microsurgery* **42**, 160–169 (2022).

84. Eser, F., Aktekin, L. A., Bodur, H. & Atan, C. Etiological factors of traumatic peripheral nerve injuries. *Neurol. India* **57**, 434 (2009).

85. Bellamkonda, R. V. Peripheral nerve regeneration: an opinion on channels, scaffolds and anisotropy. *Biomaterials* **27**, 3515–3518 (2006).

86. Nemati Mahand, S. et al. Application of stem cells, growth factors, small molecules, and biological macromolecules on nerve regeneration: a review and future direction. *Int. J. Polym. Mater. Polym. Biomater* **73**, 817–849 (2024).

87. Langer, R. & Folkman, J. Polymers for the sustained release of proteins and other macromolecules. *Nature* **263**, 797–800 (1976).

88. Rhine, W. D., Hsieh, D. S. & Langer, R. Polymers for sustained macromolecule release: procedures to fabricate reproducible delivery systems and control release kinetics. *J. Pharm. Sci.* **69**, 265–270 (1980).

89. Udin, S. B. & Scherer, W. J. Restoration of the plasticity of binocular maps by NMDA after the critical period in Xenopus. *Science* **249**, 669–672 (1990).

90. Cline, H. T., Debski, E. A. & Constantine-Paton, M. N-methyl-D-aspartate receptor antagonist desegregates eye-specific stripes. *Proc. Natl Acad. Sci.* **84**, 4342–4345 (1987).

91. Schlaggar, B. L., Fox, K. & O'Leary, D. M. Postsynaptic control of plasticity in developing somatosensory cortex. *Nature* **364**, 623–626 (1993).

92. Smith, A. L., Cordery, P. M. & Thompson, I. D. Manufacture and release characteristics of Elvax polymers containing glutamate receptor antagonists. *J. Neurosci. Methods* **60**, 211–217 (1995).

93. Puri, D. & Wagner, W. Epigenetic rejuvenation by partial reprogramming. *BioEssays* **45**, 2200208 (2023).

94. Agarwal, M. et al. Myosin heavy chain-embryonic regulates skeletal muscle differentiation during mammalian development. *Development* **147**, dev184507 (2020).

95. Clow, C. & Jasmin, B. J. Brain-derived neurotrophic factor regulates satellite cell differentiation and skeltal muscle regeneration. *Mol. Biol. Cell* **21**, 2182–2190 (2010).

96. Ahuja, P. et al. Muscle-generated BDNF (brain derived neuro-trophic factor) maintains mitochondrial quality control in female mice. *Autophagy* **18**, 1367–1384 (2022).

97. Arosio, B. et al. Sarcopenia and Cognitive Decline in Older Adults: Targeting the Muscle–Brain Axis. *Nutrients* **15**, 1853 (2023).

98. Personius, K. E. & Parker, S. D. TrkB expression at the neuromuscular junction is reduced during aging. *Muscle Nerve* **47**, 532–538 (2013).

99. Kulakowski, S. A., Parker, S. D. & Personius, K. E. Reduced TrkB expression results in precocious age-like changes in neuromuscular structure, neurotransmission, and muscle function. *J. Appl. Physiol.* **111**, 844–852 (2011).

100. Wehrwein, E. A., Roskelley, E. M. & Spitsbergen, J. M. GDNF is regulated in an activity-dependent manner in rat skeletal muscle. *Muscle Nerve: Off. J. Am. Assoc. Electrodiagn. Med.* **26**, 206–211 (2002).

101. Sakuma, K. & Yamaguchi, A. The recent understanding of the neurotrophin's role in skeletal muscle adaptation. *J. Biomed. Biotechnol.* **2011**, 201696 (2011).

102. Fu, A. K., Ip, F. C., Lai, K. O., Tsim, K. W. & Ip, N. Y. Muscle-derived neurotrophin-3 increases the aggregation of acetylcholine receptors in neuron–muscle co-cultures. *Neuroreport* **8**, 3895–3900 (1997).

103. Wells, D. G., McKechnie, B. A., Kelkar, S. & Fallon, J. R. Neuro-trophins regulate agrin-induced postsynaptic differentiation. *Proc. Natl Acad. Sci.* **96**, 1112–1117 (1999).

104. Shahini, A., Mistriotis, P., Asmani, M., Zhao, R. & Andreadis, S. T. NANOG restores contractility of mesenchymal stem cell-based senescent microtissues. *Tissue Eng. Part A* **23**, 535–545 (2017).

105. Li, X. et al. NANOG improves type I collagen expression in human fetal scleral fibroblasts. *Arch. Biol. Sci.* **71**, 63–70 (2019).

106. Singhal, N. & Martin, P. T. Role of extracellular matrix proteins and their receptors in the development of the vertebrate neuromuscular junction. *Developmental Neurobiol.* **71**, 982–1005 (2011).

107. Yurchenco, P. D., Amenta, P. S. & Patton, B. L. Basement membrane assembly, stability and activities observed through a developmental lens. *Matrix Biol.* **22**, 521–538 (2004).

108. Lifante, J. et al. Early in vivo detection of denervation-induced atrophy by luminescence transient nanothermometry. *J. Biophotonics* **17**, e202300249 (2024).

109. Sawano, S. et al. Up-and Downregulated Genes after Long-Term Muscle Atrophy Induced by Denervation in Mice Detected Using RNA-Seq. *Life* **13**, 1111 (2023).

110. Baumann, C. W., Liu, H. M. & Thompson, L. V. Denervation-induced activation of the ubiquitin-proteasome system reduces skeletal muscle quantity not quality. *PLoS One* **11**, e0160839 (2016).

111. Simpson, D. J., Olova, N. N. & Chandra, T. Cellular reprogramming and epigenetic rejuvenation. *Clin. Epigenetics* **13**, 1–10 (2021).

112. Piazzolla, D. et al. Lineage-restricted function of the pluripotency factor NANOG in stratified epithelia. *Nat. Commun.* **5**, 4226 (2014).

113. Minty, G. et al. aNMJ-morph: a simple macro for rapid analysis of neuromuscular junction morphology. *R. Soc. Open Sci.* **7**, 200128 (2020).

114. Arnold, W. D. et al. Electrophysiological motor unit number estimation (MUNE) measuring compound muscle action potential (CMAP) in mouse hindlimb muscles. *JoVE*, e52899 https://doi.org/10.3791/52899 (2015).

115. Dobin, A. et al. STAR: ultrafast universal RNA-seq aligner. *Bioinformatics* **29**, 15–21 (2013).

116. Rosenthal, R., McGranahan, N., Herrero, J., Taylor, B. S. & Swanton, C. DeconstructSigs: delineating mutational processes in single tumors distinguishes DNA repair deficiencies and patterns of carcinoma evolution. *Genome Biol.* **17**, 1–11 (2016).

117. Liao, Y., Smyth, G. K. & Shi, W. The Subread aligner: fast, accurate and scalable read mapping by seed-and-vote. *Nucleic Acids Res.* **41**, e108 (2013).

118. Love, M. I., Huber, W. & Anders, S. Moderated estimation of fold change and dispersion for RNA-seq data with DESeq2. *Genome Biol.* **15**, 1–21 (2014).

119. Subramanian, A. et al. Gene set enrichment analysis: a knowledge-based approach for interpreting genome-wide expression profiles. *Proc. Natl Acad. Sci.* **102**, 15545–15550 (2005).

120. Ashburner, M. et al. Gene ontology: tool for the unification of biology. *Nat. Genet.* **25**, 25–29 (2000).

121. Thomas, P. D. et al. PANTHER: Making genome-scale phylogenetics accessible to all. *Protein Sci.* **31**, 8–22 (2022).

122. Roballo, K. C., Burns, D. T., Ghnenis, A. B., Osimanjiang, W. & Bushman, J. S. Long-term neural regeneration following injury to the peroneal branch of the sciatic nerve in sheep. *Eur. J. Neurosci.* **52**, 4385–4394 (2020).

123. Lee, J. J. et al. Systematic interrogation of angiogenesis in the ischemic mouse hind limb: vulnerabilities and quality assurance. *Arteriosclerosis, Thrombosis, Vasc. Biol.* **40**, 2454–2467 (2020).

Acknowledgements

Author contributions

Surgeries were performed by K.E.P. Experiments were planned and designed by P.M., K.E.P. and S.T.A. Experimental data were generated and collected by P.M., K.E.P., S.S., J.T., J.J., S.B.U., and N.R. Nerve sectioning labeling was performed by C.W.H., R.E., G.K. and K.C.S.R. RNA sequencing analysis was performed by P.M., Y.Z., J.W. and S.L. Data analysis and interpretation were performed by P.M., K.E.P. and S.T.A. Writing and critical revisions of the manuscript were performed by P.M., K.E.P. and S.T.A.

Competing interests

The authors declare no competing interests.

Additional information

Supplementary information The online version contains supplementary material available at https://doi.org/10.1038/s41467-024-53276-4.

Correspondence and requests for materials should be addressed to Stelios T. Andreadis or Kirkwood E. Personius.

Peer review information *Nature Communications* thanks Ashok Kumar, and the other, anonymous, reviewer(s) for their contribution to the peer review of this work. A peer review file is available.

Reprints and permissions information is available at http://www.nature.com/reprints

Publisher's note Springer Nature remains neutral with regard to jurisdictional claims in published maps and institutional affiliations.